UNIVERSITY OF CALIFORNIA
Los Angeles

Modeling and estimation of transient two-phase thermofluid systems: an example of oscillating heat pipes

A dissertation submitted in partial satisfaction
of the requirements for the degree
Doctor of Philosophy in Mechanical Engineering

by

Yuxuan Li

2024

© Copyright by

Yuxuan Li

2024

ABSTRACT OF THE DISSERTATION

Modeling and estimation of
transient two-phase thermofluid systems:
an example of oscillating heat pipes

by

Yuxuan Li
Doctor of Philosophy in Mechanical Engineering
University of California, Los Angeles, 2024
Professor Jeffrey D. Eldredge, Co-Chair
Professor Adrienne G. Lavine, Co-Chair

Transient thermal system management is promising in various engineering disciplines such as thermal management of electronics [CKK98] and aerospace systems [DYB17]. There is a need for an approach to estimate the system's complex status to exert control and perform design optimization. Such an approach should have a low calculation cost while capturing the essential flow physics such as the phase change heat transfer and nucleate boiling. As a representative of transient thermal systems, Oscillating Heat Pipes (OHPs) consist of a serpentine capillary channel partially filled with liquid that is embedded in a thermally-conducting solid. The model reported here aims to capture the essential physics of an OHP with minimal complexity and treats some parameters typically derived from correlations or experiments (such as the film thickness and film triple point velocity) as functions with tunable constants to be estimated by data assimilation. This model contains two modules. The first uses a novel and flexible formulation of the conducting solid, solving the two-dimensional heat equation in a thin plate, with evaporators and condensers as im-

mersed forcing terms and the OHP channel as an immersed line source. The second module solves one-dimensional fluid motion and heat transfer equations within the fluid-filled channels based on mass, momentum, and energy conservation, nucleate boiling, and bubble dryout. It extends the commonly-used film evaporation-condensation model, allowing both variable liquid film thickness and length and thereby enabling the model to capture dryout. These modules are weakly coupled, in that wall temperature in the channels is obtained from the first module and heat flux from the channels determines the line source strength. After minimal training, the thermal conductance calculated by this model shows good agreement with a wide range of experiments performed by Drolen et al. [DWT22]. In particular, the model successfully predicts the experimentally-observed transition from stable OHP operation to dryout, for the first time to the authors' knowledge. Then the model is used to study the gravity effects of a ground-tested OHP and explored possible reasons of the discrepancy between the simulation and the ground experiments. This thesis also shows some data-assimilation techniques performed, such as using ensemble-Kalman Filter to estimate condenser contact condutance using a simple model adapted from Zhang et al. [ZFS02] and using Markov Chain Monte-Carlo method to sample inertial thickening parameters and plate thickness using the proposed model.

The dissertation of Yuxuan Li is approved.

Jason L. Speyer

Timothy S. Fisher

Adrienne G. Lavine, Committee Co-Chair

Jeffrey D. Eldredge, Committee Co-Chair

University of California, Los Angeles

2024

TABLE OF CONTENTS

LIST OF FIGURES

LIST OF TABLES

ACKNOWLEDGMENTS

I like this chapter, because this is a part of the thesis where I can express feelings and emotions and don't need to worry about logics. I had a fantastic 5-year journey here. I would like to firstly thank my advisor Jeff Eldredge, who introduced me to a brand new (to me) world of fluid mechanics since my first visit in the summer of 2018 (and greeting me outside in a 100-degree weather!). I would also like to thank my advisor Adrienne Lavine, who introduced me to another brand-new world of heat transfer, (I know, not very different from fluid mechanics but I never took any heat transfer courses beforehand). Also, I would like to thank you, my advisor Bruce Drolen for sharing your abundant knowledge and great questions you asked. (there are still some I haven't explored yet). And thank you my advisor Tim Fisher. I still remember your emphasize on "big pictures", your deep vision for my project, and your humorous during our group meeting. I would also like to thank Prof. Jason Speyer, both for your great courses and the book on stochastic estimations and constructive questions as my thesis committee member.

I thank my lab colleagues Ruizhi, Yi-jui, Mathieu, Diederik, Sanjay, Hanieh, and Zhecheng, my collaborator Zachary Wong, my prelim exam preparation squad member Zihao, Anthony, and Vedasri. I also thank my friends here.

I thank my parents Jun and Hanhan and my grandparents, for your unconditional love, financial and mental support throughout the COVID and my hard times. And I thank Yunshan, my partner, for your support, and your presence. I learned a lot in fluids and heat transfer, and how to love.

VITA

2019	B.S. (Aerospace Engineering), Shanghai Jiao Tong University.
2019–2024	Research Assistant, Mechanical and Aerospace Engineering Department, UCLA.
2023–2023	Teaching Assistant, Mechanical and Aerospace Engineering Department, UCLA.

PUBLICATIONS

Li, Yuxuan, Jeff D. Eldredge, Adrienne S. Lavine, Timothy S. Fisher, and Bruce L. Drolen. "A data assimilation model of oscillating heat pipe dynamics and performance." Joint 21st IHPC and 15th IHPS Melbourne, Australia (2023).

Li, Yuxuan, Jeff D. Eldredge, Adrienne S. Lavine, Timothy S. Fisher, and Bruce L. Drolen. "A conjugate heat transfer model of oscillating heat pipe dynamics, performance, and dryout." International Journal of Heat and Mass Transfer 227 (2024): 125530.

CHAPTER 1

Introduction

1.1 Motivations

When developing a physics-based mathematical model of a thermofluid system, one usually starts from first-principles: mass, momentum, and energy conservation. One extreme of the modeling approaches is trying to resolve all scales using large degrees of freedom, such as high-fidelity grid based simulations. Another extreme is trying to use minimal degrees of freedom instead to have a fast calculation. One example of the fast calculation is circuit analogy that takes temperature as voltage and heat flow rate as current. For different physical phenomena, the requirement of the degrees of freedom vary between these two extremes. For a heat conduction problem, one can use a relatively coarse grid and large time step to solve for the temperature diffusion. The computational complexity can, however, be much higher for problems with multiscale physics and advection. To accurately capture the essential physics of a complex system with computational power constraints, we need a "medium fidelity" computational model that can handle both.

In this paper, we will use a "medium fidelity" computational model to oscillating heat pipes (OHPs) as an example. An OHP, also called a Pulsating Heat Pipe (PHP) is a complex thermofluid system containing phase change, convection, liquid film dynamics, and nucleate boiling physics. Having a "medium fidelity" OHP model can have some advantages:

1. When trying to optimize the design of an OHP, this model can solve the problem relatively fast to quickly get the thermal performance of a new design.

2. Although not in full details, the essential film dynamics and nucleate boiling physics are

still reasonably included. These physics are critical to assess the OHP's thermal performance and operation limits.

3. For these essential physics included in the "medium fidelity" model, there are more parameters that are hard to measure experimentally compared with high-fidelity simulations. Data-assimilation can be performed to estimate these parameters at a lower cost than high-fidelity simulations.

1.2 Oscillating Heat Pipes

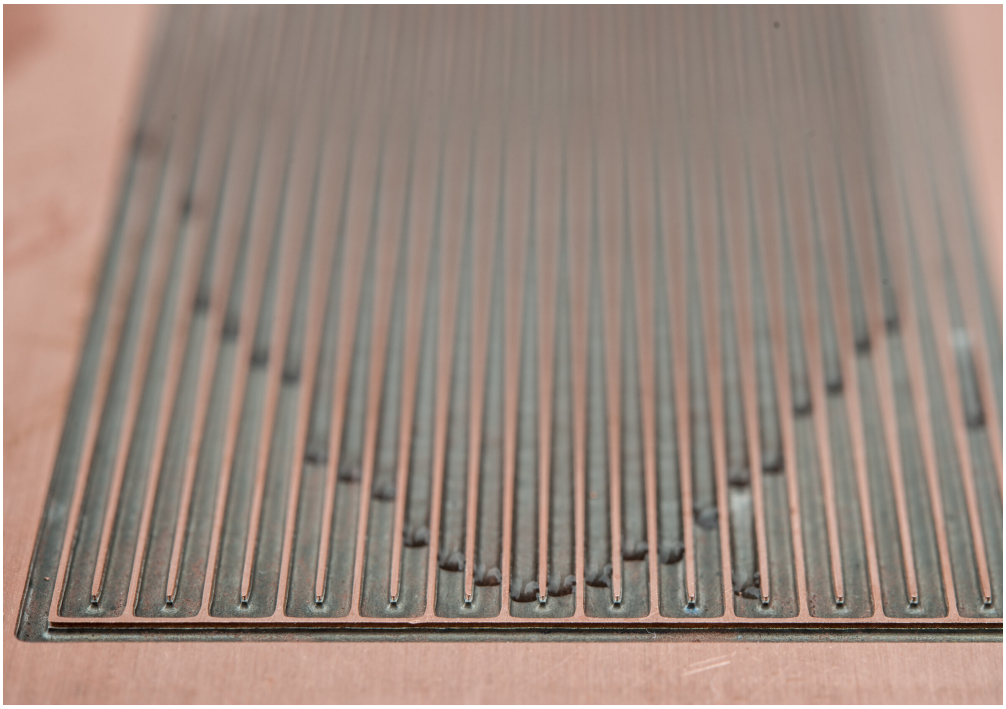

Figure 1.1: An example of an OHP (https://www.thermavant.com/ohp-heat-spreaders)

The OHP was first introduced as a device for heat transfer enhancement by Akachi [Aka90]. An OHP usually consists of a serpentine capillary channel partially filled with a working fluid, in which multiple liquid slugs and vapor bubbles (sometimes called "plugs") spontaneously form. When a heat load is applied, both evaporation and condensation phase change can occur, affecting local

vapor pressures at the evaporator and condenser. The pressure difference then drives liquid slugs away from the evaporator. Meanwhile, the evaporator region is replenished by liquid and vapor from the condenser. Overall, the liquid slugs act as "pistons" that are pushed by two adjacent vapor bubbles. This oscillation process differs uniquely from conventional heat pipes and helps an OHP achieve a low thermal resistance. Moreover, without the wick structures of a conventional heat pipe, an OHP can be much lighter, smaller, and easier to manufacture. These features provide the OHP with significant advantages for cooling electronics and aerospace systems [TS17].

OHPs display an attribute, noted by Drolen and Smoot [DS17], wherein at a given power level, they perform well (i.e., exhibit no dryout) when the heat source is physically small, but as the heat source area increases (for the same power), they exhibit dryout at the end of the heated region farthest from the condenser, undermining the device's performance. For example, in the experimental ASETS-II study (Drolen et al. [DWT22]), the OHP2 configuration, consisting of a condenser at one end, performed well when it was heated with the small heater (0.5 in $\times$ 0.5 in) at all power levels (10-40 W), with no signs of dryout. For the large heater (2 in $\times$ 2 in), the performance was consistently good at 10 W and 20 W, but some tests showed signs of partial dryout at 30 W and significantly more of the tests showed partial dryout at 40 W. This behavior is contrary to what would be expected for a conventional constant conductance heat pipe. In that device, one would expect to see good performance when the heat flux is low (large heater) and possibly poor performance as the heat flux increases (small heater) if the heat flux approaches the boiling limit.

Therefore, a central challenge for physics-based modeling of OHP performance is to capture the transition from nominal (good) to limiting (e.g., dryout) behavior. In the particular case of the ASETS-II studies, our primary objective in this work is to demonstrate a predictive model that offers good agreement with experimental data at all power levels for OHP1, for both small and large heaters, and for OHP2 with the small heater, with no indications of dryout, and, with the same model except for a change to large heater area, captures the incipient dryout at power levels of 30 W and full dryout at 40 W in OHP2. To better understand the detailed behaviors inside the channels that are hard to measure from experiments, it is important to have a physics-based model

that can predict the performance and the dry-out phenomena, in order to guide the future design of OHPs.

Although OHPs are relatively new members of the heat pipe family, there have been extensive modeling studies in the last few decades. A recent paper by Nikolayev provides a comprehensive review [Nik21]. Most models are consistent in their treatments of liquid slug dynamics, bubble nucleation, and slug fusion due to condensation. However, one difference is the treatment of liquid films along the tube wall adjacent to the vapor bubbles, a critical aspect of dryout. In earlier models, there was either no film [SFZ01] or the film was assumed to cover the entire length of the vapor region with a pre-determined thickness [HF05]. Das et al. [DNL10] proposed a film evaporation–condensation (FEC) model for a single-branch OHP. This model has a film of constant thickness but time-varying length at each end of the vapor bubble. The FEC model can thus simulate the emergence of a dry spot. Daimaru et al. [DYN17] used the FEC model for multi-branch OHPs, with a constant and uniform film thickness set a priori and showed good agreement with experiments and dry spot temperatures. Rao et al. [RLK15] extended the FEC model to allow both time varying film length and thickness. This extended model requires prior knowledge of the film's triple point velocity, a value obtained from experiment. Zhang et al. [ZN23] recently proposed an oscillating film thickness (OFT) model that allows time-varying liquid film thickness and predicts the triple point velocity deterministically. This model is validated with single-branch OHP experiments. Unlike the FEC model, the OFT model derives the triple point velocity from local contact angle and superheat properties rather than the total mass flow of the liquid film. Such a model includes more detailed physics at the end of the liquid film. With lumped film length and thickness, the FEC model and OFT model are examples with a balance between low complexity and essential physics for the dry spot and film heat transfer.

Nemati et al. [NS18] introduced an explicit one-dimensional film model by discretizing the film into finite elements. This approach is likely more realistic because it allows multiple dry spots to emerge in one vapor bubble. However, with more degrees of freedom, greater complexity is added to the computations.

The development of liquid film models allowing dry spots in vapor bubbles greatly enhanced the study of dry-out phenomena in OHPs. Senjaya and Inoue [SI14] meshed all liquids, vapors, and liquid films as small control volumes and numerically studied a two-turns OHP for the first 30 s. They concluded that dryout occurs easily in the simulation without vapor bubble generation and does not occur with vapor bubble generation. Nekrashevych and Nikolayev [NN17] used an approach with effective evaporators and condensers to enable multiple dry spots within one vapor bubble to simulate dryout on start-up. They showed that dryout can also occur with bubble generation. And in their subsequent work [NN19] for a 300-second simulation of a 10-turn copper-water OHP, they show that dryout occurs when power exceeds a thershold level for all horizontally and vertically mounted OHPs. To the best of our knowledge, there have been no quantitative experimental validations of dryout in multi-branch OHP models.

In the present paper, we will report a simple but flexible film model for multi-branch OHP systems that keeps the advantage of simplicity and efficiency from the FEC model and extends it by enabling time-varying liquid film thickness and length. It still approximates the triple point velocity from a fraction of the total mass flow of the liquid film, see Section 2.1.6, like the FEC model. The value of this fraction is considered uncertain and applies to all liquid films.

In addition to uncertainties in film length and thickness variations with phase change, there is also uncertainty in the film's thickness deposited by a liquid slug. As a liquid slug travels, it deposits a film behind it (at the slug's "trailing end"). Aussillous and Quéré [AQ00] showed that in the visco-inertial regime, the film can be at most 50% thicker than Taylor's law for small capillary numbers in the Taylor-Bretherton regime. Thus, there is also an uncertainty of the relative film thickness compared with Taylor's law.

The triple point physics and film deposition thickness are among the uncertainties in a model of OHP physics, as is the bubble nucleus size that determines the critical superheat for boiling. The simulation behavior is sensitive to each and therefore they need to be approximated well.

There have been efforts to solve the conjugate heat transfer problem with more than one-dimensional heat conduction on the wall, especially for flat plate OHPs. Odagiri et al. [OWC21] solved a three

dimensional heat equation to study the thermal diffusion in the casing simultaneously and studied the dry spot. Noh et al. [NYK21] also proposed a three dimensional heat equation and concluded that when Fourier number is higher than 5×10^5, the thermal interactions between adjacent channels cannot be neglected.

In this paper, we report a model that captures two-dimensional conjugate heat transfer in a plate (averaged across the plate's thickness), nucleate boiling, and vapor bubble dry-out. In order to account for heat transfer between the capillary tube and the solid plate in which it is embedded, we use an immersed boundary method [Eld22] that enables simple meshing in the solid plate. The model parameters are initially determined by manual training from ASETS-II experimental data. Importantly, each parameter is set from limited training data and then left unchanged for further testing. Thus, the model becomes predictive after the training is completed, and we show that this predictive model shows good agreement with ASETS-II experimental results omitted from the training set. Table 1.1 shows some representative previous validations for multi-branch OHPs in comparison with present work. There are small differences between our work and previous work in terms of nucleate boiling, liquid merging, and liquid-vapor interface tracking. Our work is novel in two crucial ways. The first aspect is the manner in which the plate's heat transfer is coupled with the OHP physics (via an immersed boundary method, and an integration across the thickness direction to achieve an effectively 2D plate simulation). It enables the user of our methodology to reconfigure the OHP in the plate without any change whatsoever to the plate's mesh. Second, to our knowledge, no previous OHP modeling investigation has quantitatively validated their model with experiments on the transition from stable operation to dryout, as we have in this study.

references	wall	layouts/cases	comparison values	validation period
Abela et al. [AMN22]	1D	1/7	T_w, V_l, L_l	start-up
Daimaru et al. [DNA17]	1D	1/3	T_w	stable
Odagiri et al. [OWC21]	3D	1/4	T_w	stable
Bae et al. [BLK17]	1D	3/>100	T_w	stable
Rouaze et al. [RMC21]	1D	2/41	T_w	stable
Noh et al. [NYK21]	3D	5/41	T_w	stable
present work	2D	4/16	T_w	start-up and stable, with dryout

Table 1.1: Previous experimental validations for multi-branch OHPs

CHAPTER 2

Model Formulation

Four configurations are studied as shown in Figure 2.1. These OHPs are identical in construction, except that OHP1 has condensers on both sides while OHP2 only has a condenser on one side. Each configuration has four heater power levels (10 W, 20 W, 30 W, and 40 W). Thus in total sixteen cases are simulated. Although OHP2 experimental cases do not have condensers on the left end by design, this nominally adiabatic side is supported by G-10 fiberglass and bolts. In the simulation we place an adiabatic side condenser indicated in light blue with a very low effective heat transfer coefficient to account for possible heat leakage through the bolts and radiation. We will still refer to this side as the adiabatic side. For detailed experimental setup readers can refer to Drolen et al.'s work [DWT22].

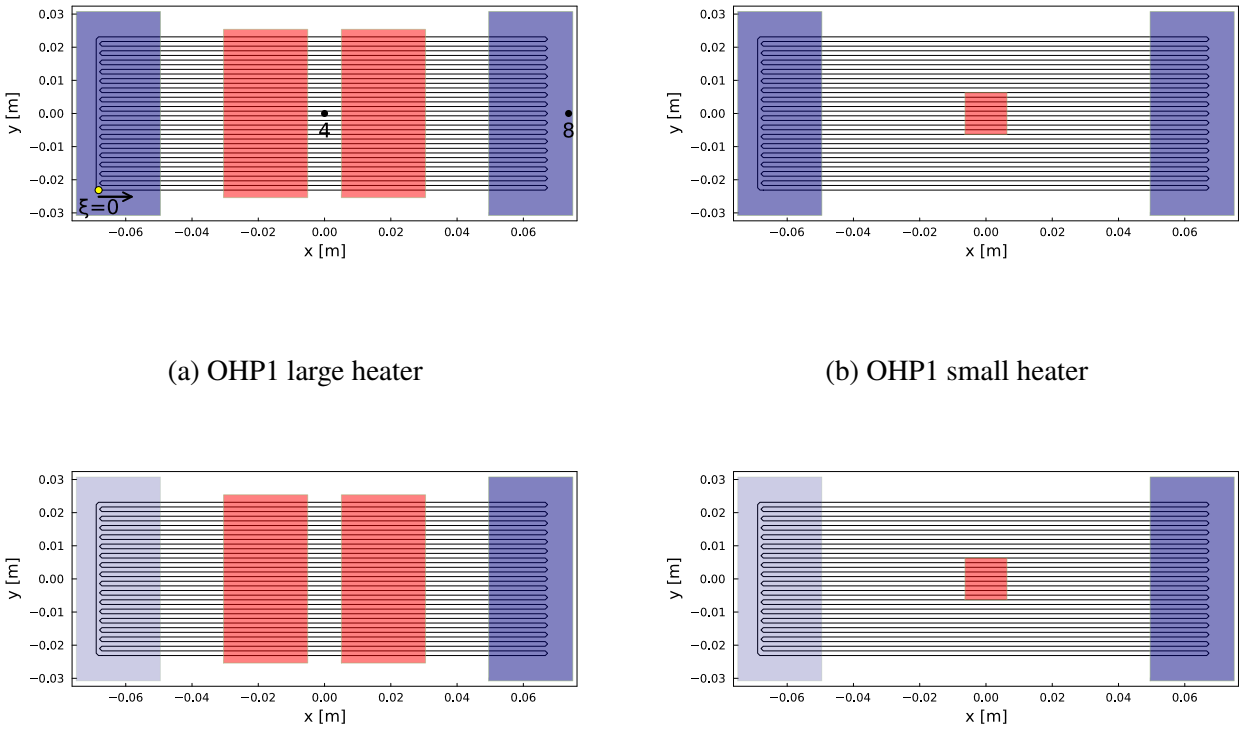

(a) OHP1 large heater

(b) OHP1 small heater

(c) OHP2 large heater

(d) OHP2 small heater

Figure 2.1: Dimensions and layouts of serpentine channels (black), evaporators (red), condensers (dark blue), and adiabatic side condensers (light blue)

In this section, we describe the formulation of the OHP model used in this paper. We first describe the fluid model, which includes the liquid slug, vapor bubble, and liquid film treatments in the OHP capillary tubes. Then we describe the solid model, consisting of heat transfer within the plate and thermal coupling between the solid and fluid models via the immersed boundary method.

The fluid model uses a stationary one-dimensional mesh for the wall and a moving mesh for each liquid slug. It uses the 4th order Runge-Kutta scheme for time marching. And the solid model uses a two dimensional Cartesian grid and the alternating-direction implicit (ADI) method to solve the unsteady heat equation.

2.1 Fluid Model

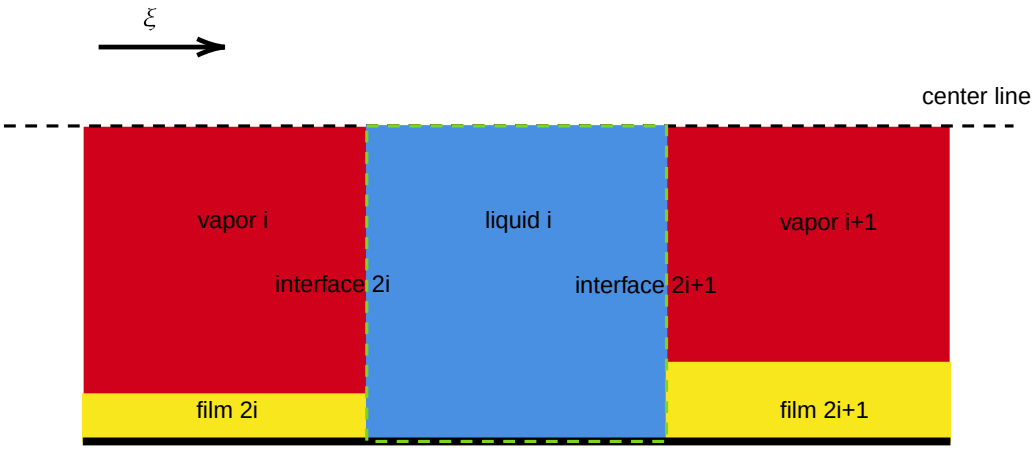

Figure 2.2: System of labels and indices of the OHP slug/vapor/film model.

The OHP is composed of a series of liquid slugs and vapor bubbles. The channels are square. Liquid films may exist between each vapor bubble and the wall. The fluid model considers mass and energy transfer within and between the vapor bubble, the film, and the liquid slug, as well as the momentum equation for the slug. The system of labels and indices are shown in Figure 2.2. For a closed loop OHP, the number of liquid slugs equals the number of vapor bubbles, and the number of liquid films and interfaces are twice the number of liquid slugs. The fluid model is coupled to a model of conduction in the wall, by taking the wall temperature from the solid model as a boundary condition. It then returns the wall heat flux to the solid model. The coupling with the solid model is described in the following section; here, we focus only on the fluid model. Table 2.1 shows the fluid and tube properties used in this paper. Liquid properties and interface properties (surface tension and latent heat) are chosen at 291.2 K and do not vary during the simulation. 291.2 K is a typical experiment initial temperature. butane is the experiments' typical working fluid. Note that vapor properties still vary in the model.

New vapor bubbles can be generated from nucleate boiling in liquid slugs when there is enough superheat and other conditions are fulfilled. Some critical parameters used for nucleate boiling such

as the nucleation site radius r_{n}, the number of nucleation sites N_{n}, and the boiling waiting time t_{wait} are listed in Table 2.2. Although the former two parameters are common to see in previous work, the boiling waiting time is introduced in the current work to account for the time a vapor bubble needs to grow for every nucleation station. The vapor bubble can also disappear when two liquid slugs merge. The detailed algorithms for nucleate boiling and merging can be found in Section 2.1.7.

symbols	physical meaning	unit	value
ρ_{l}	liquid density	$\mathrm{kg/m^3}$	5.81×10^2
μ_{l}	liquid dynamic viscosity	kg/m s	1.69×10^{-4}
k_{l}	liquid thermal conductivity	W/m K	1.08×10^{-1}
σ	surface tension	N/m	1.27×10^{-2}
h_{lv}	latent heat	J/kg	3.68×10^5
D_{w}	tube hydraulic diameter	m	1×10^{-3}
P_{w}	tube perimeter	m	4×10^{-3}
A_{w}	tube cross-sectional area	$\mathrm{m^2}$	1×10^{-6}

Table 2.1: Properties table for butane and the tube, reference temperature is $T = 291.2\mathrm{K}$

symbols	meaning	unit	value
	initial liquid slug number		30
h_{c}	condenser effective heat transfer coefficient	$\mathrm{W/m^2\ K}$	2.3×10^3
$h_{\mathrm{adia,c}}$	adiabatic side condenser effective heat transfer coefficient	$\mathrm{W/m^2\ K}$	1.61×10^2
L_{merge}	vapor bubble length threshold for merging	m	3×10^{-3}
L_{insert}	inserted vapor bubble length for boiling	m	6×10^{-3}
r_{n}	nucleation site radius	m	3×10^{-6}
t_{wait}	boiling waiting time	s	1
N_{n}	number of nucleation sites		250
$\varepsilon / D_{\mathrm{w}}$	relative roughness		1×10^{-3}
w_δ	film thickness factor		1.3
η_+	film dynamics parameter for positive heat flux		0.6
η_-	film dynamics parameter for negative heat flux		0

Table 2.2: Uncertain parameters used for the simulation

2.1.1 Mass Conservation and Velocities of Liquid-Film Interface

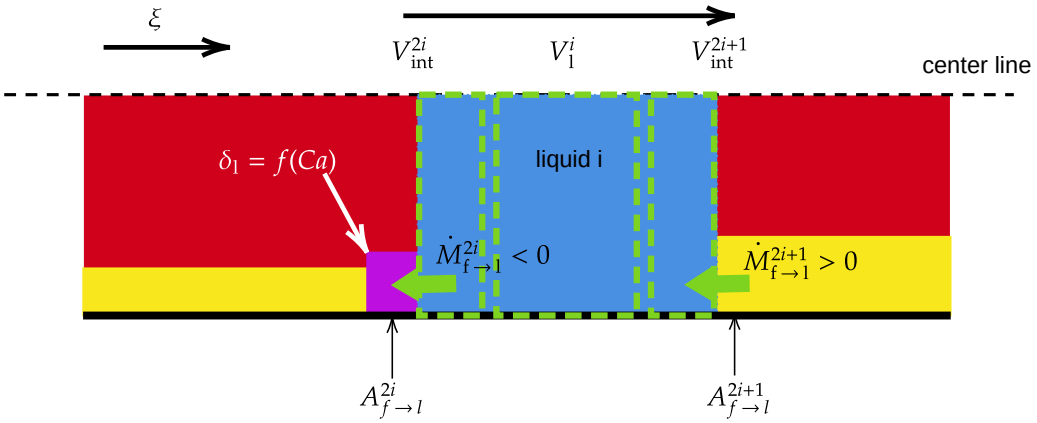

Figure 2.3: Mass Conservation

The average velocity field across the cross-section is called the bulk velocity, $V_{\mathrm{l}}^{(i)}$. When a liquid slug moves, there will be mass flux into or out of it from two films: one that is deposited behind it (from the slug's "trailing end") and another in front of it (at the slug's "leading end") that it absorbs. Because the liquid slug is picking up liquid film on the leading edge and releasing a different liquid film on the trailing edge, for each liquid slug i (as shown in Figure 2.3), the two interfaces' velocities $V_{\mathrm{int}}^{(2i)}$ and $V_{\mathrm{int}}^{(2i+1)}$ are not generally equal to each other nor to the slug's bulk velocity $V_{\mathrm{l}}^{(i)}$. For simplicity, each interface is idealized as a planar surface parallel to the cross-section, and the velocity within the film is assumed to be zero since it is adjacent to the wall and the drag from the vapor bubble is small. (Note that all velocities are defined relative to the wall.)

In 2.1.2, we apply conservation of mass to the slug to derive the relationships between the bulk and interface velocities and to the mass flow rates between the slug and the films at each end, using the control volumes shown as dashed green boxes in Figure 2.3. The interface velocities are

$$\left(A_{\mathrm{w}} - A_{\mathrm{f}\to\mathrm{l}}^{(j)}\right) V_{\mathrm{int}}^{(j)} = A_{\mathrm{w}} V_{\mathrm{l}}^{(i)}, \tag{2.1}$$

where $j = 2i$ or $2i + 1$. j stands for the index of interfaces. $\dot{M}_{\mathrm{f}\to\mathrm{l}}^{(j)}$ is the mass flow rate from film j into the attached liquid slug,

$$\dot{M}_{\mathrm{f}\to\mathrm{l}}^{(j)} = (-1)^{j+1} \rho_{\mathrm{l}} V_{\mathrm{int}}^{(j)} A_{\mathrm{f}\to\mathrm{l}}^{(j)}, \tag{2.2}$$

where $A_{\mathrm{f}\to\mathrm{l}}^{(j)}$ can be understood as a characteristic film cross-sectional area. Each film's interface with the slug has a corresponding $A_{\mathrm{f}\to\mathrm{l}}^{(j)}$.

There are three cases where $A_{\mathrm{f}\to\mathrm{l}}^{(j)}$ is defined. For example, let us imagine a liquid slug moves from left to right in Figure 2.3:

Case1: At the leading end of the liquid slug we have $\dot{M}_{\mathrm{f}\to\mathrm{l}}^{(2i+1)} > 0$, and the film section closest to the interface is absorbed by the slug. Thus $A_{\mathrm{f}\to\mathrm{l}}^{(2i+1)}$ is chosen as the cross-sectional area of the side of the leading film $(2i + 1)$ adjacent to the interface.

Case2: At the leading end of the liquid slug, when the leading film is dry, $\dot{M}_{\mathrm{f}\to\mathrm{l}}^{(2i+1)} = 0$, and thus $A_{\mathrm{f}\to\mathrm{l}}^{(2i+1)} = 0$.

Case3: At the trailing end of the slug, the slug leaves behind a new section of the trailing film $(2i)$ and we expect $\dot{M}_{\mathrm{f}\to\mathrm{l}}^{(2i)} < 0$. This newly deposited segment of film does not need to have the same cross-sectional area as the film farther to the left.

We assume that all newly deposited films have the same thickness, δ_{l}, which is determined based on the wetting behavior of thin liquid films left behind a droplet moving in a capillary tube [AQ00]:

$$\delta_{\mathrm{l}} = \frac{D_{\mathrm{w}}}{2} \frac{1.34\mathrm{Ca}^{2/3}}{1 + 3.35\mathrm{Ca}^{2/3}} w_{\delta}. \tag{2.3}$$

The Capillary number Ca is defined as

$$\mathrm{Ca} = \frac{\mu_{\mathrm{l}} |V|_{avg}}{\sigma}, \tag{2.4}$$

where $|V|_{avg}$ is the average absolute interface velocity of liquid slugs at each time step. In the current model one time-varying Capillary number is used for all liquid slugs at one instant to ensure computational efficiency. μ_{l} is the dynamic viscosity of liquid, σ is the surface tension, and w_{δ} is the film thickness factor that compensates for the effect of inertial thickening. In the current model w_{δ} is manually tuned, as explained in Section 3. Its value is in Table 2.2. Note that the "nascent" film thickness δ_{l} (depicted as the purple section in Figure 2.3) derived here does not consider phase change and it is not the actual liquid film thickness $\delta^{(j)}$. The phase change effects and the liquid motion mass flow rate discussed in this section are both considered in equation (2.26) to finally determine actual film thickness $\delta^{(j)}$.

In this paper, we idealize all films to have a uniform thickness (within one vapor bubble) around the perimeter of the tube, and thus for case 1, the cross-sectional area of any film $A_{\mathrm{f}\to\mathrm{l}}^{(j)} \approx \delta^{(j)} P_{\mathrm{w}}$, where $\delta^{(j)}$ is the film's thickness. For case 3, this relation also applies to the "nacsent" film released by the liquid slug and we have $A_{\mathrm{f}\to\mathrm{l}}^{(j)} \approx \delta_{\mathrm{l}}^{(j)} P_{\mathrm{w}}$, where $\delta_{\mathrm{l}}^{(j)}$ is the "nascent" film thickness. For the square-channel configuration used in this paper, $P_{\mathrm{w}} = 4D_{\mathrm{w}}$ is the square tube's perimeter.

The formulation in this section does not *require* each film to be of uniform thickness along the tube's axis in each vapor bubble, but the model has been *implemented* with uniform thickness films. Note, however, that the film thickness can change with time (see Section 2.1.6). Based on the above

analysis, $A_{\mathrm{f}\to\mathrm{l}}^{(j)}$ can be written as

$$\frac{A_{\mathrm{f}\to\mathrm{l}}^{(j)}}{A_{\mathrm{w}}} = \begin{cases} \dfrac{4\delta^{(j)}(D_{\mathrm{w}} - \delta^{(j)})}{D_{\mathrm{w}}^2}, & \dot{M}_{\mathrm{f}\to\mathrm{l}}^{(j)} > 0, \quad \text{wet leading film} \\ 0, & \dot{M}_{\mathrm{f}\to\mathrm{l}}^{(j)} = 0, \quad \text{dry leading film} \\ \dfrac{4\delta_{\mathrm{l}}(D_{\mathrm{w}} - \delta_{\mathrm{l}})}{D_{\mathrm{w}}^2}, & \dot{M}_{\mathrm{f}\to\mathrm{l}}^{(j)} < 0, \quad \text{trailing film.} \end{cases} \tag{2.5}$$

2.1.2 Liquid Slug and the Liquid-Vapor Interface

This section describes in more detail our model for the liquid slug and its interface with the adjacent vapor regions and liquid films. We will refer to Figure 2.3 for the derivation that follows.

At any instant, we regard each liquid slug i as principally composed of a bulk region, surrounded by two interface regions at the leading $(2i + 1)$ and trailing $(2i)$ ends of the slug. These interface regions are associated with mass exchanges between the slug and the adjacent films, over areas $A_{\mathrm{f}\to\mathrm{l}}^{(2i+1)}$ and $A_{\mathrm{f}\to\mathrm{l}}^{(2i)}$, respectively. Consistent with our film model, we approximate the liquid velocity as zero over these slug-film interfaces. Furthermore, the liquid is assumed to completely fill the channel over all three regions, as indicated in Figure 2.3. We also recall that, in our model, we ignore direct phase change at the slug-vapor interface.

The axial momentum of slug i is defined as

$$M_{\mathrm{l}}^{(i)} V_{\mathrm{l}}^{(i)} = \int_0^{L_{\mathrm{l}}^{(i)}} \int_{A_{\mathrm{w}}} \rho_{\mathrm{l}} u \, \mathrm{d}A \mathrm{d}\xi, \tag{2.6}$$

where $M_{\mathrm{l}}^{(i)}$ and $V_{\mathrm{l}}^{(i)}$ are the mass and the mass-averaged velocity of the slug, respectively, $L_{\mathrm{l}}^{(i)}$ represents the length of the slug and A_{w} the cross-sectional area of the channel, and u is the axial velocity distribution of the liquid across the cross section of the slug.

Since the liquid is assumed incompressible with uniform density,

$$M_{\mathrm{l}}^{(i)} = \rho_{\mathrm{l}} A_{\mathrm{w}} L_{\mathrm{l}}^{(i)}, \tag{2.7}$$

and the area integral of u is independent of ξ, as can be confirmed by applying conservation of mass

in any stationary control volume in the slug. Thus,

$$A_{\mathrm{w}} V_{\mathrm{l}}^{(i)} = \int_{A_{\mathrm{w}}} u \, \mathrm{d}A. \tag{2.8}$$

In other words, $V_{\mathrm{l}}^{(i)}$ also represents the area-averaged velocity across any cross-section of the slug.

At the liquid-vapor interfaces at the leading and trailing ends of the slug, the stationary film requires that this area-averaged velocity is distributed across the smaller areas $A_{\mathrm{w}} - A_{\mathrm{f}\to\mathrm{l}}^{(j)}$, for $j = 2i+1$ and $2i$, respectively. We define the corresponding average liquid velocities of these interfaces as $V_{\mathrm{int}}^{(j)}$, such that

$$\left(A_{\mathrm{w}} - A_{\mathrm{f}\to\mathrm{l}}^{(j)}\right) V_{\mathrm{int}}^{(j)} = A_{\mathrm{w}} V_{\mathrm{l}}^{(i)} = \int_{A_{\mathrm{w}}} u \, \mathrm{d}A. \tag{2.9}$$

These are the velocities at which the interfaces are propagated in our model. Note that the mass-averaged velocity, $V_{\mathrm{l}}^{(i)}$, is necessarily smaller than the interface velocities.

With these definitions, let us inspect conservation of mass and momentum for the slug. For mass conservation, we will focus our attention on the two interface regions separately, see left and right control volumes indicated with green dashed lines in Figure 2.3 For example, at the leading end of the slug, $2i+1$, let us make use of the rightmost control volume that extends across the channel and whose right boundary moves uniformly at velocity $V_{\mathrm{int}}^{(2i+1)}$ and whose left boundary moves at velocity $V_{\mathrm{l}}^{(i)}$. The only flux of mass into the control volume is through the film interface, equal to

$$\dot{M}_{\mathrm{f}\to\mathrm{l}}^{(2i+1)} = \rho_{\mathrm{l}} V_{\mathrm{int}}^{(2i+1)} A_{\mathrm{f}\to\mathrm{l}}^{(2i+1)}, \tag{2.10}$$

since the film velocity is assumed zero. This mass flux is necessarily equal to the rate of increase of mass in the control volume, reflecting the uptake of mass by the slug at its leading end. Similarly, at the trailing end, we can make use of a control volume whose right boundary moves at velocity $V_{\mathrm{l}}^{(i)}$ and whose left boundary at $V_{\mathrm{int}}^{(2i)}$, and it is easy to verify that the mass flux into the control volume is

$$\dot{M}_{\mathrm{f}\to\mathrm{l}}^{(2i)} = -\rho_{\mathrm{l}} V_{\mathrm{int}}^{(2i)} A_{\mathrm{f}\to\mathrm{l}}^{(2i)}. \tag{2.11}$$

This flux is negative, with magnitude equal to the rate of mass loss of the slug into the trailing film.

In the bulk region, defined by the center control volume bridging the two interface control volumes just used, the mass does not change in time. We emphasize the definitions of these three regions of the slug are simply an instantaneous artifice that enables us to account for mass exchange with the films. The boundaries between these regions are not tracked over time. Furthermore, these boundaries are not material surfaces, and fluid particles can move between the regions while still preserving zero net mass flux across each boundary. It is sufficient to know that the overall rate of increase of mass in the slug is equal to the sum of the two mass fluxes, (2.10) and (2.11).

2.1.3 Liquid Momentum

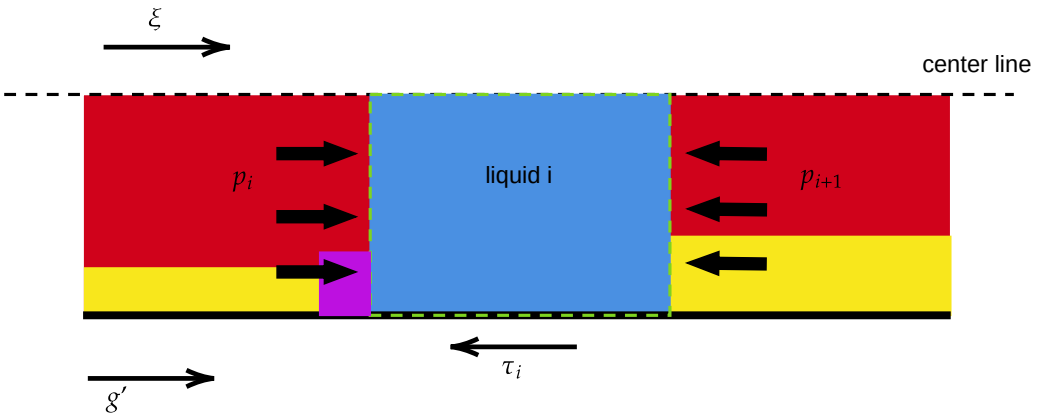

Figure 2.4: Liquid slug momentum equation schematic

For conservation of momentum in the slug, we dispense with the three separate control volumes and instead rely on an overall control volume that combines them, moving at the leading and trailing ends with velocities $V_{\text{int}}^{(2i+1)}$ and $V_{\text{int}}^{(2i)}$, respectively. Because of our assumption of zero velocity in the film, there is no momentum flux into or out of this control volume. The rate of change of momentum in the slug, $M_{\text{l}}^{(i)} V_{\text{l}}^{(i)}$, is therefore equal to the sum of the forces on the slug. This is expressed in equation (2.12).

With reference to Figure 2.4, we apply conservation of momentum to the slug in 2.1.2. This

results in

$$\frac{\mathrm{d}(M_\mathrm{l}^{(i)}V_\mathrm{l}^{(i)})}{\mathrm{d}t} = \left(p_\mathrm{v}^{(i)} - p_\mathrm{v}^{(i+1)}\right) A_\mathrm{w} - \rho_\mathrm{l} g' \Delta H^{(i)} A_\mathrm{w} - P_\mathrm{w} L_\mathrm{l}^{(i)} \tau_\mathrm{l}^{(i)}, \tag{2.12}$$

where $M_\mathrm{l}^{(i)}$ is the mass of liquid slug i, $V_\mathrm{l}^{(i)}$ is the cross-sectionally averaged bulk velocity of the liquid slug, $p_\mathrm{v}^{(i)}$ is the pressure of vapor i, $\Delta H^{(i)}$ is the height difference between the two interfaces, and g' is the projection of gravity g in the channel direction. For our current simulation for OHPs under microgravity, $g = 0$. $L_\mathrm{l}^{(i)}$ is the length of liquid slug i. P_w is the perimeter of the tube, and $\tau_\mathrm{l}^{(i)}$ is the axial stress in the liquid at the wall. When using a typical velocity of 0.3 m/s, the typical Reynolds number of the pipe flow is 1029. But in a few cases the Reynolds number reached 14000. To have a smooth transition from laminar flow to turbulent flow, the Churchill friction correlation [Chu77] is used to determine $\tau_\mathrm{l}^{(i)}$:

$$f = 8\left[\left(\frac{8}{\mathrm{Re}}\right)^{12} + \frac{1}{\left(\Theta_1 + \Theta_2\right)^{1.5}}\right]^{\frac{1}{12}} \tag{2.13}$$

where

$$\begin{aligned} \Theta_1 &= \left[-2.457 \ln\left(\left(\frac{7}{\mathrm{Re}}\right)^{0.9} + 0.27\frac{\varepsilon}{D_\mathrm{w}}\right)\right]^{16} \\ \Theta_2 &= \left(\frac{37530}{\mathrm{Re}}\right)^{16}. \end{aligned} \tag{2.14}$$

In the Churchill equation, the relative roughness ε/D_w can be found in Table 2.2. The value is a typical surface roughness of a machined aluminum surface and is kept constant throughout all simulations. Note that in this work, the pressure drop due to interface curvature is neglected. For the OHP after startup, for the configuration explored in this paper, the average vapor pressure difference across a representative liquid slug of an OHP ranges from 160 Pa to 1659 Pa, depending on the configurations and heating powers and with a typical value at 500 Pa. Using the Young–Laplace equation, assuming the radius of curvature to be 0.5 mm (half of the tube diameter), the pressure drop across one interface is 50 Pa, which is 10 % of the typical pressure difference. If considering two interfaces, they counteract each other and reduce the net effect of curvature when $Ca \ll 1$

[CKK15] (suitable for our case considering a typical velocity of 0.3 m/s). But this simplification should be used with caution if one studies an OHP at a low power level.

2.1.4 Liquid Energy

For each liquid slug i, an independent cross-sectionally averaged one-dimensional energy equation is solved. This equation can be derived with a control volume of infinitesimal axial length that moves with the liquid bulk velocity, in the bulk region as defined in 2.1.2. The resulting equation is

$$\rho_{\mathrm{l}} c_{\mathrm{p,l}} A_{\mathrm{w}} \frac{\partial T_{\mathrm{l}}}{\partial t} = k_{\mathrm{l}} A_{\mathrm{w}} \frac{\partial^2 T_{\mathrm{l}}}{\partial x^2} + P_{\mathrm{w}} q''_{\mathrm{w}}(x), \tag{2.15}$$

where x is an axial coordinate defined in the moving slug, $c_{\mathrm{p,l}}$ is the specific heat of the liquid, k_{l} is the thermal conductivity of the liquid, and T_{l} is the cross-sectionally averaged liquid temperature. Because this equation is written using a coordinate fixed to the moving slug, there is no advection term. $q''_{\mathrm{w}}(x)$ is the wall heat flux into the liquid at x. At any given time, $q''_{\mathrm{w}}(x)$ can be expressed as

$$q''_{\mathrm{w}}(x) = h_{\mathrm{l}} \left[T_{\mathrm{w}}(\xi(x)) - T_{\mathrm{l}}(x) \right], \tag{2.16}$$

where $\xi(x)$ is a mapping from the slug's moving coordinate system to the fixed axial coordinate in the OHP wall, and h_{l} is the heat transfer coefficient for all liquid slugs,

$$h_{\mathrm{l}} = \mathrm{Nu}_{\mathrm{l}} \frac{k_{\mathrm{l}}}{D_{\mathrm{w}}}, \tag{2.17}$$

and the Nusselt number is $\mathrm{Nu}_{\mathrm{l}} = 3.60$, corresponding to laminar flow in a square duct with a uniform heat-flux boundary condition [SL14].

2.1.5 Vapor Model

In the model, the vapor is assumed to be saturated, so that

$$p_{\mathrm{v}}^{(i)} = p_{\mathrm{sat}}(\rho_{\mathrm{v}}^{(i)}), \quad T_{\mathrm{v}}^{(i)} = T_{\mathrm{sat}}(\rho_{\mathrm{v}}^{(i)}) \tag{2.18}$$

where $\rho_{\mathrm{v}}^{(i)}$ is the density of vapor i, which is defined from the vapor mass divided by the vapor volume, both of which are tracked. The assumption that the vapor bubble is at saturation conditions is an approximation that is supported by our separate (unreported) investigation, in which we solved the full vapor bubble energy equation. This approximation makes the model considerably more efficient computationally, with little sacrifice in physical fidelity. Our model emphasizes more on predicting the onset of dry-out and the thermal performance before dry-out.

The saturation curve for obtaining the conditions in (2.18) is derived from the CoolProp package [BWQ14]. For each vapor bubble, two liquid films are assumed to be located at its two ends. (see Figure 2.5). Heat transfer between the wall and the vapor in the dry regions (vapor regions not covered by films) is neglected. Each film j has a time varying but spatially uniform thickness $\delta^{(j)}$ and a time varying length predicted by the model, as described below. The two films can meet in the middle of the bubble. Phase change at bubble-slug interfaces at the two ends is neglected because the bubble-slug (cross-sectional) interface area is small compared to the bubble-film (peripheral) interface area. The conduction across the bubble-slug interface is still accounted and will cause but takes only a tiny portion of phase-change of the liquid film. The heat transfer across the liquid film is assumed to occur only by conduction, and the film is assumed thin compared to the tube edge length. Thus heat transfer is calculated as if the film were planar:

$$q_{\mathrm{f}}''^{(j)}(\xi) = \frac{k_{\mathrm{l}}}{\delta^{(j)}} \left(T_{\mathrm{w}}(\xi) - T_{\mathrm{v}}^{(i)} \right). \tag{2.19}$$

Here, $q_{\mathrm{f}}''^{(j)}(\xi)$ represents the heat flux at a given location ξ on film j. The total heat transfer rate due to phase change at the film-vapor interface for film j can then be found as

$$q_{\mathrm{f}}^{(j)} = \int_{\mathrm{f}}^{(j)} P_{\mathrm{w}} q_{\mathrm{f}}''^{(j)}(\xi) \mathrm{d}\xi. \tag{2.20}$$

The corresponding evaporation (or condensation) mass flow rate for film j can then be expressed as:

$$\dot{M}_{\mathrm{f}\to\mathrm{v}}^{(j)} = \frac{q_{\mathrm{f}}^{(j)}}{h_{\mathrm{lv}}}, \tag{2.21}$$

where h_{lv} is the latent heat. As noted previously, phase change at the bubble-slug interface is neglected.

The net mass flow rate into the vapor i from the leading and trailing liquid film can be expressed as

$$\dot{M}_{\mathrm{v}}^{(i)} = \dot{M}_{\mathrm{f}\to\mathrm{v}}^{(2i-1)} + \dot{M}_{\mathrm{f}\to\mathrm{v}}^{(2i)}. \tag{2.22}$$

This information is used to track the density within the bubble as a function of time, in order to determine saturation temperature and pressure using Equation (2.18).

2.1.6 Film Length and Thickness

An actual liquid film has a complex interface shape. However, for simplicity, we assume the film to have a rectangular shape, described by two scalar dimensions, $L_{\mathrm{f}}^{(j)}$ and $\delta^{(j)}$, as shown in Figure 2.5. The purpose of this FEC model is to mimic the high-dimensional liquid film dynamics globally while retaining low complexity.

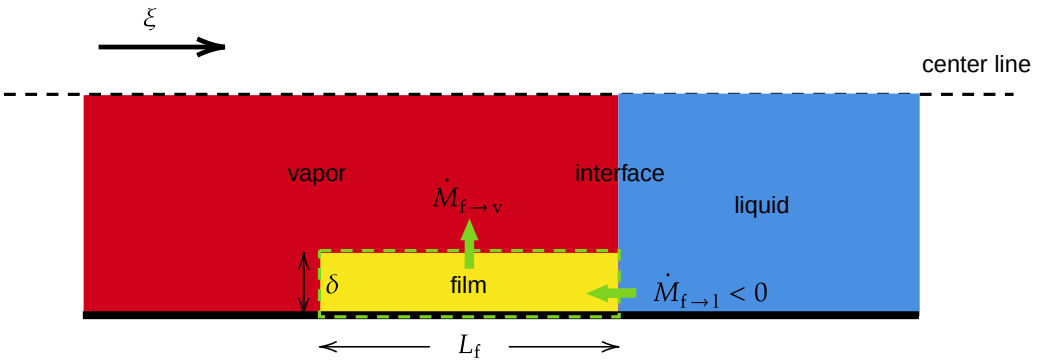

Figure 2.5: Film mass conservation

From mass conservation, the mass change of a film comes from phase change and interface motion. This relation can be written as

$$\dot{M}_{\mathrm{f}}^{(j)} = -\dot{M}_{\mathrm{f}\to\mathrm{v}}^{(j)} - \dot{M}_{\mathrm{f}\to\mathrm{l}}^{(j)}, \tag{2.23}$$

where $\dot{M}^{(j)}_{\mathrm{f}\to\mathrm{v}}$ is the phase change mass flow rate and $\dot{M}^{(j)}_{\mathrm{f}\to\mathrm{l}}$ is the interface deposition mass flow rate into, or out of, the liquid slug. Using Eqs. (2.2) and (2.21), the $\dot{M}^{(j)}_{\mathrm{f}}$ are determined.

However, knowledge of the mass change of the film as a whole is insufficient. When mass flux enters or exits the film, it simultaneously changes the film's length and thickness. Using the product law for the mass change of film $M^{(j)}_{\mathrm{f}} = \rho_{\mathrm{l}} A^{(j)}_{\mathrm{f}} L^{(j)}_{\mathrm{f}}$ and assuming that the liquid is incompressible:

$$\dot{M}^{(j)}_{\mathrm{f}} = \rho_{\mathrm{l}} L^{(j)}_{\mathrm{f}} \dot{A}^{(j)}_{\mathrm{f}} + \rho_{\mathrm{l}} A^{(j)}_{\mathrm{f}} \dot{L}^{(j)}_{\mathrm{f}} \tag{2.24}$$

where $A^{(j)}_{\mathrm{f}}$ is the cross-sectional area of film j. Note that the film thickness, $\delta^{(j)}$, can be derived from $A^{(j)}_{\mathrm{f}}$.

In addition to Equation (2.24), another constraint is required to derive $\dot{A}^{(j)}_{\mathrm{f}}$ and $\dot{L}^{(j)}_{\mathrm{f}}$. This constraint can be imposed by specifying the percentage contribution from the mass flow rate on the triple line at the end of the liquid film. We will introduce a weighting function $\eta^{(j)}(\xi)$ to explain them in the following paragraphs. We hypothesize that this contribution is determined only by the working liquid and wall properties. For example, the analysis and experiments of Rao et al. [RLK15] showed that, for water in evaporation, the contribution of the mass flow rate at the triple line can be $\sim 1/3$ of the total mass flow rate. In our analysis, we do not presume this percentage, but rather, determine it indirectly from the overall experimental OHP results, along with other uncertain parameters. With reference to equations (2.20), (2.21), and (2.23), we propose the following forms for each mass flow rate in (2.24):

$$\rho_{\mathrm{l}} A^{(j)}_{\mathrm{f}} \dot{L}^{(j)}_{\mathrm{f}} = -\frac{P_{\mathrm{w}}}{h_{\mathrm{lv}}} \int_{\mathrm{f}}^{(j)} \eta^{(j)}(\xi) q''_{\mathrm{f}} \mathrm{d}\xi + (-1)^{(j)} \rho_{\mathrm{l}} A^{(j)}_{\mathrm{f}} V^{(j)}_{\mathrm{int}} \tag{2.25}$$

$$\rho_{\mathrm{l}} L^{(j)}_{\mathrm{f}} \dot{A}^{(j)}_{\mathrm{f}} = -\frac{P_{\mathrm{w}}}{h_{\mathrm{lv}}} \int_{\mathrm{f}}^{(j)} \left(1 - \eta^{(j)}(\xi)\right) q''_{\mathrm{f}} \mathrm{d}\xi - \left(\dot{M}^{(j)}_{\mathrm{f}\to\mathrm{l}} + (-1)^{(j)} \rho_{\mathrm{l}} A^{(j)}_{\mathrm{f}} V^{(j)}_{\mathrm{int}} \right) \tag{2.26}$$

where $\eta^{(j)}(\xi)$ is a weighting function, defined as

$$\eta^{(j)}(\xi) = H(q''_{\mathrm{f}}) \eta_{+} + H(-q''_{\mathrm{f}}) \eta_{-}, \tag{2.27}$$

and $H()$ is the Heaviside step function. In equation (2.25), $\rho_{\mathrm{l}} A^{(j)}_{\mathrm{f}} V^{(j)}_{\mathrm{int}}$ is the portion of $\dot{M}^{(j)}_{\mathrm{f}\to\mathrm{l}}$ that

goes to $\rho_l A_f^{(j)} \dot{L}_f^{(j)}$. Its presence in the equation ensures that the tail (triple line) of the film does not move without phase change. The remaining portion of $\dot{M}_{f\to l}^{(j)}$ goes to $\rho_l L_f^{(j)} \dot{A}_f^{(j)}$ in equation (2.26).

The two dimensionless numbers, η_+ and η_-, are introduced to represent the effects of the complex phase change: η_+ denotes the percentage of mass flux going to the length change where the film is evaporated ($q_f'' > 0$), and η_- denotes the percentage of mass flux going to length change where the film is condensed ($q_f'' \leq 0$). For example, if $\eta_+ = \eta_- = 0$, then phase change will never change the film's length. In contrast, if $\eta_+ = \eta_- = 1$, then the film's thickness will never change regardless of phase change. From Rao et al.'s experimental paper [RLK15], η_+ and η_- vary with flow conditions and are not constants, which is different from our simplified assumption in the next paragraph.

In the current model, all films share the same η_+ and η_-, and their values are manually tuned, as explained in Section 3. Their tuned values are reported in Table 2.2. In spite of the low dimensionality, our FEC model still allows a time varying thickness for each film and is able to distinguish the "dry" regions (the portion of the vapor bubble not covered by a film j). As we will show, this distinction is pivotal to accurately simulate the onset of dry-out. We note that, recently, there is an Oscillating Film Thickness (OFT) model that uses local temperature difference to derive the contact point velocity [ZN23]. The OFT model's favorable aspect is to make the contact point velocity independent of the film length, after some extra calculations for each contact point. This approach would be interesting to consider in future work.

2.1.7 Nucleate Boiling and Merging

The model simulates nucleate boiling by creating new vapor bubbles that break a liquid slug into two at a nucleation site. In the simulation, a finite number of nucleation sites are randomly distributed along the length of the OHP tube.

In this model, three prerequisites are needed to trigger a boiling event at a nucleation site. Firstly, the site should be in a liquid region. Secondly, the temperature difference between the wall $T_w(\xi_n)$

and the saturation temperature $T_{\mathrm{sat}}(\xi_{\mathrm{n}})$ must exceed the superheat threshold $\Delta T_{\mathrm{n,th}}$. Finally, the time interval between two boiling events at the same nucleation site should exceed the waiting time threshold t_{wait} to account for the bubble growth time.

To determine $T_{\mathrm{sat}}(\xi_{\mathrm{n}})$ at the liquid slug, first the saturation pressure $p_{\mathrm{sat}}(\xi_{\mathrm{n}})$ in the liquid slug is derived by linearly interpolating the saturation pressures of the adjacent vapor bubbles. Then the saturation temperature can be derived from the Clausius-Clapeyron equation. The superheat threshold $\Delta T_{\mathrm{n,th}}$ is derived from an equation from [QM07]:

$$\Delta T_{\mathrm{n,th}} = T_{\mathrm{sat}}\left(\xi_{\mathrm{n}}\right)\left(\frac{f\left(\xi_{\mathrm{n}}\right)}{1-f\left(\xi_{\mathrm{n}}\right)}\right), \tag{2.28}$$

where

$$f(\xi_{\mathrm{n}}) = \frac{R T_{\mathrm{sat}}\left(\xi_{\mathrm{n}}\right)}{h_{\mathrm{lv}}} \ln\left[1+\frac{2\sigma}{p_{\mathrm{sat}}\left(\xi_{\mathrm{n}}\right)}\left(\frac{1}{r_{\mathrm{n}}}-\frac{1}{D_{\mathrm{w}}-2\delta_{\mathrm{n}}}\right)\right] \tag{2.29}$$

and r_{n} is the nucleation site radius, R is the gas constant, σ is the surface tension, and δ_{n} is the Taylor bubble's film thickness. In the simulation δ_{n} is neglected because it is at least one order of magnitude smaller than D_{w}. A more detailed description of the boiling process is given in Algorithm 1. t_{wait} and r_{n} are manually tuned as explained in Section 3. Their values are in Table 2.2.

Algorithm 1: Nucleate boiling

Input: $vapor$, $liquid$, $T_{\mathrm{sat}}\left(\xi_{\mathrm{n}}^{(k)}\right)$, $T_{\mathrm{w}}\left(\xi_{\mathrm{n}}^{(k)}\right)$, L_{insert}

Output: new $vapor$, new $liquid$

for $k = 1$ *to* N_{n} **do**

  if $\left(T_{\mathrm{w}}\left(\xi_{n}^{(k)}\right) - T_{\mathrm{sat}}\left(\xi_{n}^{(k)}\right)\right) > \Delta T_{\mathrm{n,th}}$ *and* $\xi_{n}^{(k)} \in \mathrm{C}_{\mathrm{liquid}}$ *and* $\Delta t_{\mathrm{boil}} > t_{\mathrm{wait}}$ **then**

    insert a new vapor bubble i **at** $\xi_{n}^{(k)}$:

    `// insert new vapor pressure`

    $p_{\mathrm{v}}^{(i)} \leftarrow p_{\mathrm{sat}}\left(T_{\mathrm{w}}\left(\xi_{\mathrm{n}}^{(k)}\right)\right)$;

    `// create two interfaces`

    $\xi_{\mathrm{int}}^{(2i-1)} \leftarrow \xi_{n}^{(k)} - L_{\mathrm{insert}}/2$;

    $\xi_{\mathrm{int}}^{(2i)} \leftarrow \xi_{n}^{(k)} + L_{\mathrm{insert}}/2$;

    `// Velocity of liquid slugs remain unchanged`

    $V_{\mathrm{l}}^{(i)} \leftarrow V_{\mathrm{l,old}}^{(i)}$

  end

end

Similar to the nucleate boiling process that creates new vapor bubbles, a merging function is used to remove a vapor bubble if two liquid slugs collapse. The approach for merging is given in Algorithm 2.

Algorithm 2: Liquid slug merging

Input: *vapor*, *liquid*, L_{merge}

Output: new *vapor*, new *liquid*

for $i = 1$ *to* N_{v} **do**
  if $L_{\text{v}}^{(i)} < L_{\text{merge}}$ **then**
    remove vapor bubble i:
    `// move two liquid slugs together`
    $\xi_{\text{int}}^{(2i-2)} \leftarrow \xi_{\text{int,old}}^{(2i-2)} + L_{\text{v}}^{(i)}/2;$
    $\xi_{\text{int}}^{(2i-1)} \leftarrow \xi_{\text{int,old}}^{(2i+1)} - L_{\text{v}}^{(i)}/2;$
    `// get the new` $V^{(i-1)}$ `from momentum conservation.`
    $V_{\text{l}}^{(i)} \leftarrow V_{\text{l,old}}^{(i)}$
  end
end

L_{insert} and L_{merge} are manually tuned in Section 3. Their values are in Table 2.2. They are also limited by the interface velocities and the numerical time step.

2.2 Solid Model and Its Coupling to the OHP

symbols	physical meaning	unit	value
ρ_s	density	kg/m^3	2.73×10^3
c_s	specific heat	J/kg K	8.93×10^2
k_s	thermal conductivity	W/m K	1.93×10^2
d_s	average plate thickness	m	1.5×10^{-3}
Δt_{step}	simulation time step	s	4×10^{-4}
L_x	OHP length	m	1.524×10^{-1}
L_y	OHP width	m	6.48×10^{-2}
N_x	grid number in x direction		250
N_y	grid number in y direction		110
N_w	number of nodes on the tube wall		4877
	fill ratio	%	46

Table 2.3: Solid properties and simulation parameters

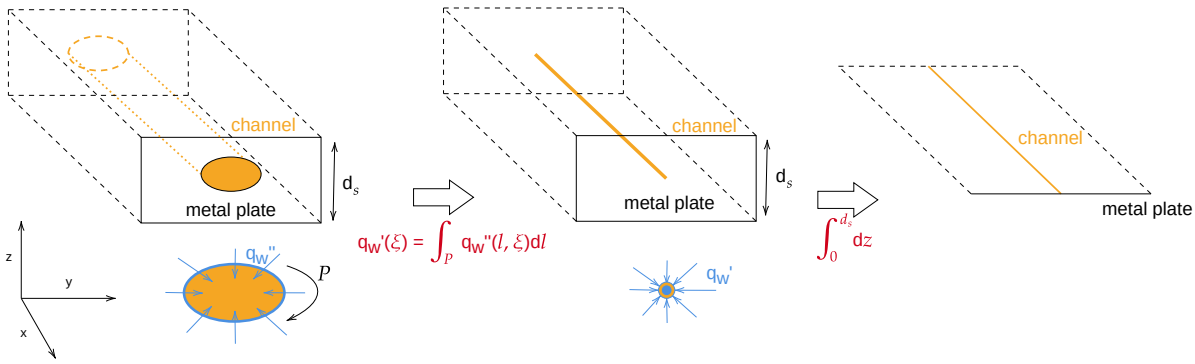

Figure 2.6: Schematic of transforming the full three-dimensional plate heat transfer model (left) to a three-dimensional model with immersed OHP (center) and, finally, a two-dimensional immersed OHP model (right).

The OHP channel is embedded into a solid plate. The full three-dimensional heat equation in the plate $\Omega \subset \mathbb{R}^3$ is

$$\rho_s c_s \frac{\partial T_s}{\partial t} = k_s \left(\frac{\partial^2 T_s}{\partial x^2} + \frac{\partial^2 T_s}{\partial y^2} + \frac{\partial^2 T_s}{\partial z^2} \right), \qquad (x, y, z) \in \Omega \subset \mathbb{R}^3, \tag{2.30}$$

where z represents the thickness direction. In addition to this equation, along the edges of the plate we set adiabatic boundary conditions. On the top and bottom of the plate we enforce conditions for the adjacent evaporators and condensers. Both of these conditions are modeled via surface heat flux conditions. That is, we set

$$\mp k_s \frac{\partial T_s}{\partial z} = q'', \tag{2.31}$$

where q'' denotes the heat flux into the plate, and where the $-$ sign is chosen at the bottom surface and $+$ at the top surface of the plate. However, the models for this heat flux differ for evaporators and condensers. Evaporators are modeled as prescribed heat fluxes, $q''_h = W_h / A_h$, where power W_h is delivered over a surface region of area A_h. Condensers, in contrast, are modeled as reservoirs of constant temperature, so that the surface heat flux over the condenser region is given by $q''_c = h_c(T_c - T_s)$, and the effective heat transfer coefficient h_c is assumed constant.

Heat transfer in the solid and OHP fluid are coupled at the OHP channel wall. If the full shape and size of the channel were resolved in the solid model, then the local heat flux q''_w through the channel wall from solid to fluid would be introduced as another boundary condition for Equation (2.30), as depicted schematically in the left panel of Figure 2.6. Correspondingly, the local plate temperature at the channel wall would be provided as a boundary condition for the OHP model. One would construct a mesh that conforms to the channel wall in order to introduce these conditions into the discretized equations.

However, in order to obtain a more computationally efficient model, we perform two simplifications. First, we assume that the diameter of the channel is sufficiently small compared to x and y dimensions of the plate (length and width) that, from the perspective of the plate, the heat from the plate to the OHP channel can be thought of as collecting into a *line heat sink* concentrated along

the serpentine length of the OHP channel (the center panel in Figure 2.6). The local strength of the heat sink is given by the heat transfer per unit length through the perimeter of the channel, P_w,

$$q'_w(\xi) = \int_{P_w} q''_w(l, \xi)\, \mathrm{d}l, \tag{2.32}$$

where ξ is the arc length coordinate along the OHP channel.

As a result of this assumption, the heat transfer through the channel wall is represented not as a boundary condition but, rather, as a volumetric heating term on the right side of Equation (2.30), of the form

$$q'''_s = -\int_{C_{OHP}} q'_w(\xi)\, \delta_{3D}\left(\underline{x} - \underline{x}(\xi)\right) \mathrm{d}\xi, \tag{2.33}$$

where $\delta_{3D}()$ is the three-dimensional Dirac delta function and $\underline{x}(\xi)$ describes the curve of the OHP channel centerline. The negative sign ensures the positive sign convention we have used for heat flux, into the OHP from the plate. In other words, the OHP is immersed into the plate's volume, and the computational mesh does not need to conform to the channel's shape [Eld22]. The volume integral of (2.33) over the region surrounding the OHP achieves an identical heat transfer rate compared to the original surface integral over the OHP channel wall (since the integral of the delta function is equal to 1 over this volume), regardless of the original shape of the channel. In addition, this assumption allows us to obtain the local channel wall temperature, averaged over the perimeter, from the temperature in the plate evaluated at the OHP centerline, $T_w(\xi) = T(\underline{x}(\xi))$.

The second simplification we make is to integrate the full three-dimensional equation (2.30) with respect to z over the thickness d_s of the plate (the right panel in Figure 2.6). It becomes

$$\rho_s c_s d_s \frac{\partial \overline{T}_s}{\partial t} = k_s d_s \left(\frac{\partial^2 \overline{T}_s}{\partial x^2} + \frac{\partial^2 \overline{T}_s}{\partial y^2} \right) + q'' + d_s \overline{q}'''_s, \qquad (x, y) \in \overline{\Omega} \subset \mathbb{R}^2 \tag{2.34}$$

where $\overline{T}_s$ and $\overline{q}'''_s$ are z-averaged temperature and heat source terms; the latter is

$$\overline{q}'''_s d_s = -\int_{C_{OHP}} q'_w(\xi)\, \delta_{2D}\left(\underline{x} - \underline{x}(\xi)\right) \mathrm{d}\xi \tag{2.35}$$

where $\delta_{2D}()$ is the two-dimensional Dirac delta function. Furthermore, the integral of the conductive term brings the heat flux boundary conditions for the evaporators and condensers on the top and

the bottom of the plate directly into the equation, represented collectively as q''. Note that $q'' = 0$ anywhere outside an evaporator or a condenser.

As in the three-dimensional model, the wall temperature is obtained from the local plate temperature, $T_{\mathrm{w}}(\xi) = \overline{T}_s(\underline{x}(\xi))$, which can be written alternatively as

$$T_{\mathrm{w}}(\xi) = \int_{\overline{\Omega}} \overline{T}_s\left(\underline{x}\right) \delta_{2\mathrm{D}}\left(\underline{x} - \underline{x}(\xi)\right) \mathrm{d}\underline{x}. \tag{2.36}$$

Equation (2.36) represents an interpolation of the plate temperature onto the channel's centerline.

Equation (2.34) is solved on a Cartesian grid with adiabatic boundary conditions at the plate edges. The equation is discretized in time with the Crank-Nicolson method and solved with the alternating-direction implicit method. The integrals over Dirac delta functions in these equations are represented discretely as sums over discrete Dirac delta functions [Eld22]. Table 2.3 shows the solid dimensions and properties used in this paper representing 6061 aluminum alloy.

CHAPTER 3

Results for OHPs in microgravity condition

All uncertain parameters in Table 2.2 were chosen manually to match four cases (OHP1 large heater 10W/40W and OHP2 large heater 10W/40W). Then, all remaining cases were run with the same parameter set.

3.1 Normal Operating OHP Example

This section presents the OHP1 large heater 40 W case, a representative of fully operational OHPs. Figure 3.1 shows the temperature contours of the OHP1 large heater 40 W case as predicted by the model. The first four snapshots show a temperature increase in the middle that spreads to the two ends. The last two snapshots show that the temperature field remains nearly unchanged from 100 s to 300 s. Figure 3.2 shows snapshots of liquid slug (blue) and vapor bubble distributions. It also distinguishes vapor bubbles with (yellow) and without (red) liquid films on the wall. It can be seen that the majority of the vapor bubble length is covered by liquid films (yellow) throughout the simulation.

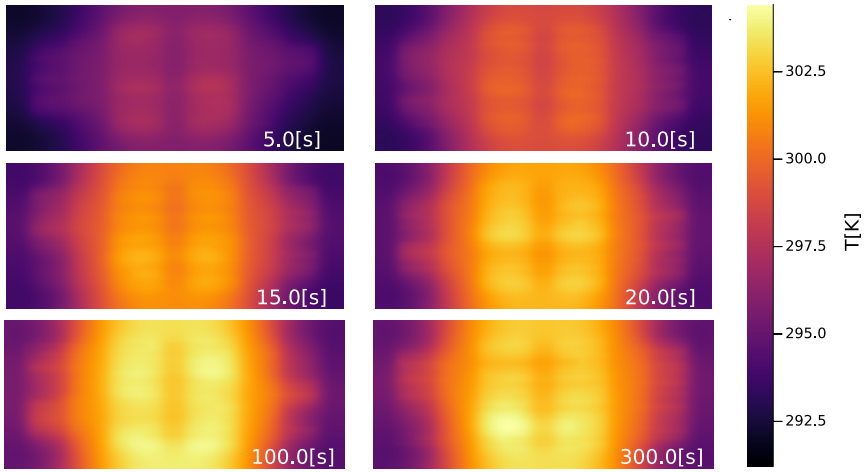

Figure 3.1: Temperature contours for OHP1 large heater 40 W

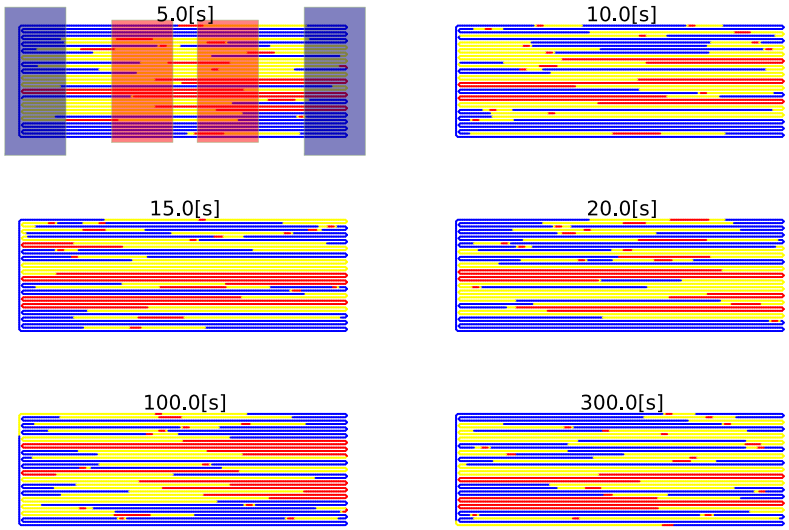

Figure 3.2: Snapshots for OHP1 large heater 40 W, blue • region is liquid, red • region is dry vapor, and yellow • region is vapor covered by liquid films. Note that the red vapor cannot be seen in yellow regions because they are wrapped by liquid films.

Figure 3.3 shows one temperature difference curve for the OHP1 large heater 40 W case with condensers at both ends. The temperature difference is the difference between T_4 and T_8. Their

locations are shown in Figure 2.1a. The current model does not have a detailed module to simulate the heat transfer between the condenser and the casing. The simulation result (one simulation represnted by the blue curve) agrees well with experiments for both the initial time dependence and the nominally steady-state results; the predicted steady-state temperature difference is within approximately 17 % of the experimental value. The temperature difference value fluctuates because of the oscillating nature of OHPs. The purple envelope of seven simulations shows that there will be a range of the OHPs' thermal performance if run multiple times, due to the randomness of initial slug and nucleation site locations. The extremum here is the actual extremum of one of the seven cases, and it is not statistical variation. The orange curve is the moving averaged overall boiling frequency from the numerical simulation. It is hard to validate this value quantitatively because boiling data are not available in the experiments. But the numerical result shows that the boiling is consistent throughout the simulation.

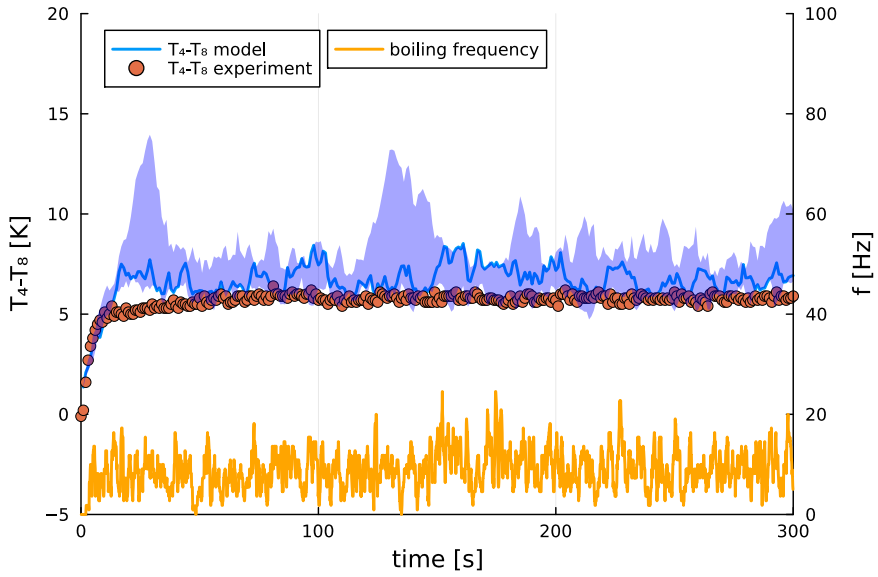

Figure 3.3: Temperature difference ($T_4 - T_8$) comparison and overall boiling frequency for OHP1 large heater 40 W case. Their locations are shown in Figure 2.1a. The purple shaded area shows the envelope of seven simulations. This 300 s simulation takes 298 minutes on a Macbook Air with a M1 chip.

3.2 Dryout OHP Example

Figure 3.4 shows the temperature contours of OHP2 large heater 40 W case. It shows that the peak temperature at 300 s is significantly higher than at 100 s, showing the runaway dryout. The runaway dryout is more evident in Figure 3.5. At 100 s, the result shows the transition to runaway dryout where more dry vapor regions are shown toward the left. And the liquid slugs tend to accumulate to the right end where the only condenser is situated. The 300 s result shows the liquid and vapor distribution after runaway dryout has occurred and most of the vapor region is dry.

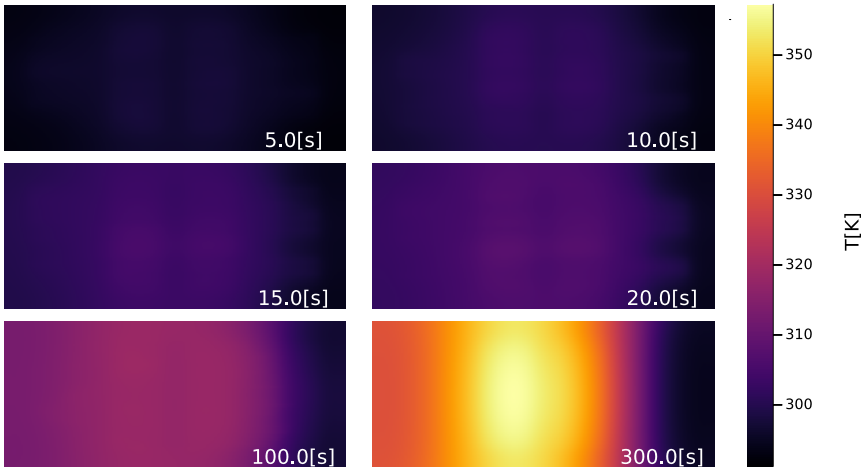

Figure 3.4: Temperature contours for OHP2 large heater 40 W

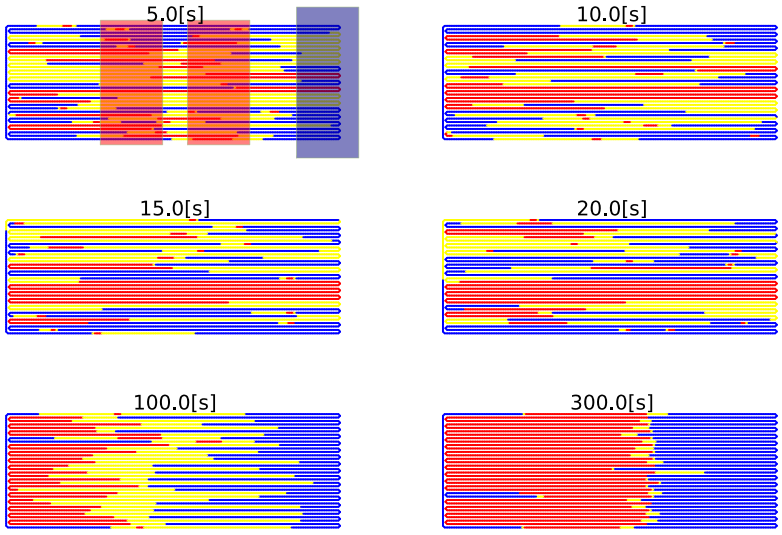

Figure 3.5: Snapshots for OHP2 large heater 40 W, blue • region is liquid, red • region is dry vapor, and yellow • region is vapor covered by liquid films

Figure 3.6 shows a representative temperature difference curve for the OHP2 large heater 40 W case with only one condenser at the right end. This is a more challenging case with the transition from normal operation to runaway dryout. Although the model slightly over-estimated the temperature difference during the transition, the simulation agrees well with experiments for the initial start-up time and successfully predicts the onset of runaway dryout. The purple envelope of seven simulations is narrow during the startup and transition, but becomes wider at later time, showing some of the cases experienced dryout while some did not prior to 300 s. The boiling frequency curve also shows that this case has a lower boiling frequency at the beginning relative to the previous curve, and the frequency dramatically decreases when there is onset of runaway dryout around 230 s.

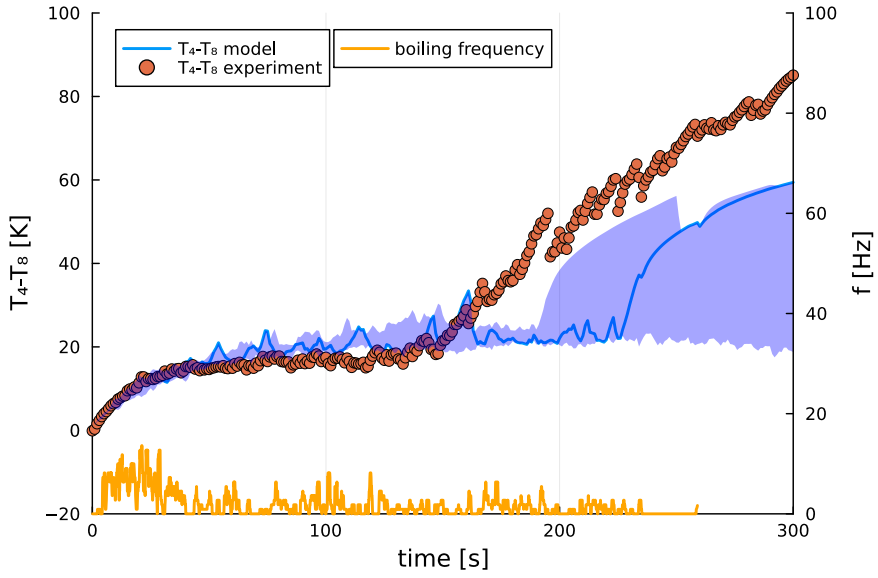

Figure 3.6: Temperature difference ($T_4 - T_8$) comparison and overall boiling frequency for OHP2 large heater 40 W case. Their locations are shown in Figure 2.1a. Purple shaded area shows the envelope of seven simulations.

3.3 ASETS-II experiments thermal conductance comparison

In this section, we will assess the OHP model on sixteen cases, comparing with experimental data where appropriate. This comparison in nominal steady-state will be based on thermal conductance. Thermal conductance is defined here as

$$G = \frac{\text{heater power}}{T_4 - T_8}, \tag{3.1}$$

where T_4 and T_8 are the interpolated temperatures from the solid model corresponding to RTD4 and RTD8 results in ASETS-II experiments [DWT22]. Their locations are shown in Figure 2.1a.

Figure 3.7 shows the time-averaged thermal conductance comparison with ASETS-II experiments for 16 cases. The values are averaged from 100 s to 200 s. The error for large heater cases is within 20 % except for the OHP1 large heater 10 W case with error of 24 %. It is also shown

that this model can predict small heater cases' thermal conductance well. The difference is within 13 % except for the OHP1 small heater 10 W case with error of 32 %, using the same parameter set calibrated for large heaters. Note that in Figure 3.7d at 40W, the red line is not an error bar, it shows the transition from normal operation to dryout after 200s.

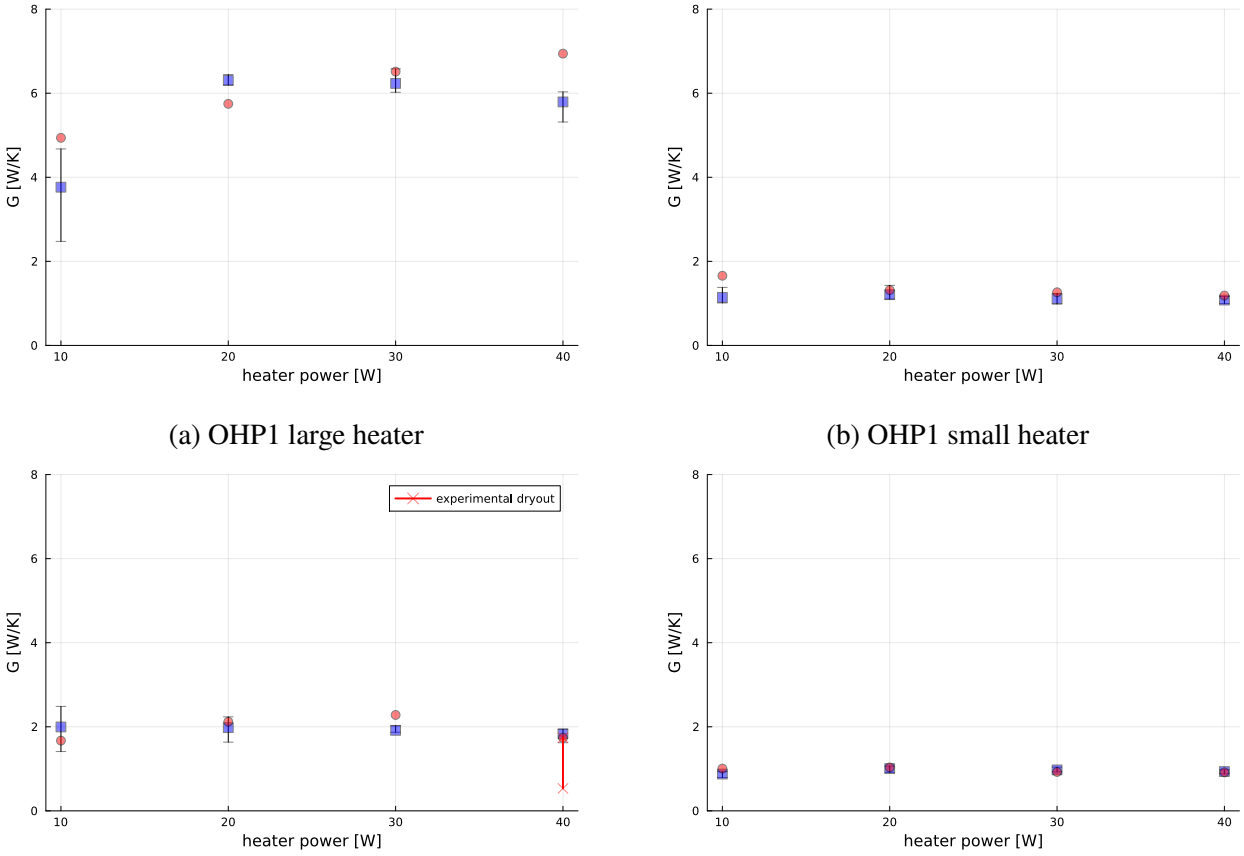

(a) OHP1 large heater

(b) OHP1 small heater

(c) OHP2 large heater

(d) OHP2 small heater

Figure 3.7: Averaged thermal conductance comparison, red circles ● are experimental thermal conductance, and blue squares ■ are time-averaged numerical thermal conductance averaged over seven simulations. The error bars show the range of time-averaged thermal conductance over seven simulations.

3.4 Other numerical results

Figure 3.8 shows the time history of liquid and film motions for three representative cases. Each vertical slice of this figure represents a snapshot of an OHP in one-dimensional coordinates. In other words, the serpentine channels shown in Figures 3.2 and 3.5 have been stretched out along the vertical direction in Figure 3.8. Figure 3.8a shows a normal operating large heater OHP's time history. It shows random oscillatory patterns and relatively small dry vapor regions. Figure 3.8b shows a normally operating OHP2 small heater OHP's time history. OHP1 small heater in Figure 3.8c shows similar patterns (not shown here). Figure 3.8b shows a time-varying dry spot in the channels under and in close proximity to the heater. The oscillatory patterns are still random but less so than in Figure 3.8a. Figure 3.8d shows a dryout case. It can be seen that there are random oscillations initially. After around 50 s, the liquid slugs move to the condenser section and tend to only oscillate around the condenser. This relatively confined oscillation can be seen from 50 s to around 230 s. Starting from approximately 230 s, the red stripes show that the majority of the vapor regions become dry. And in the meantime the blue stripes show that the liquid slugs' amplitude of oscillations are greatly reduced. When taking a closer look at the dry-out case, in Figure 3.8e, the blue rectangles on the right end show the locations of the condensers and red rectangles stand for evaporators. They show that the transitions between evaporators and condensers occured around 8 times for OHP2 large heater case per meter (in 1D coordinates). It is shown that before dry-out occurs, the liquid slugs were undergoing large amplitude oscillations and sometimes extending under the evaporators. And over time, the amplitude of oscillations became smaller and finally dry-out occurred. The mechanism of why dry-out only occurs at higher power levels is still unresolved, but the current model is able to capture this phenomenon that agrees with the ASETS-II experiment.

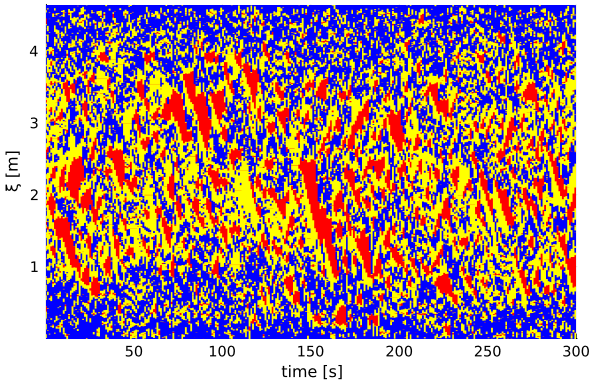

(a) OHP1 large heater 40 W

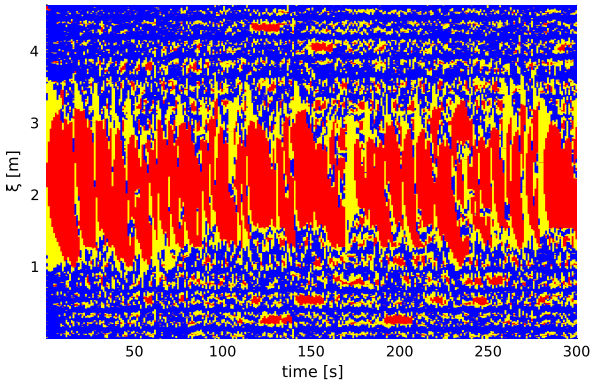

(b) OHP2 small heater 40 W

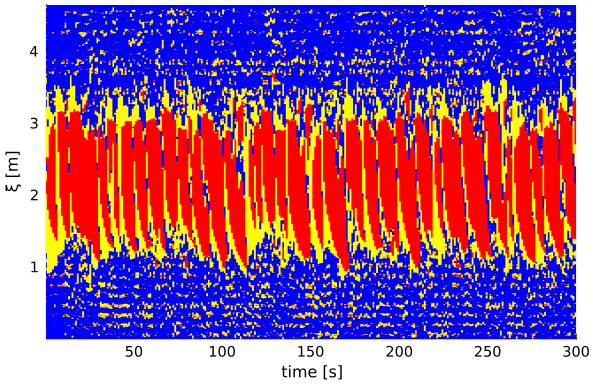

(c) OHP1 small heater 40 W

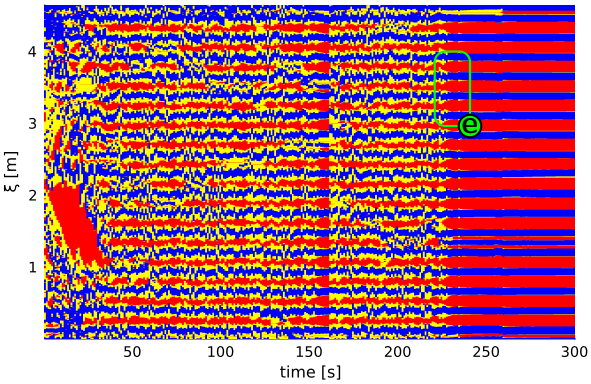

(d) OHP2 large heater 40 W (The green box means the time and ξ range of Figure 3.8e)

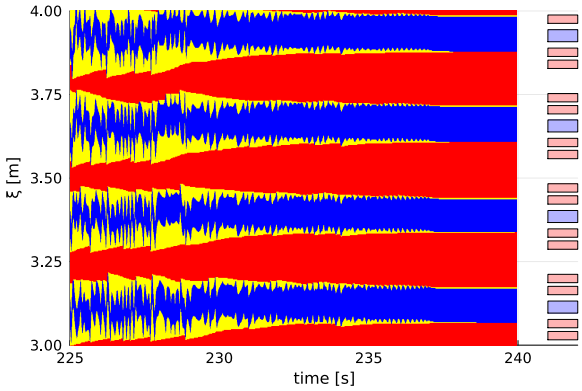

(e) OHP2 large heater 40 W dryout closer view, see green box in Figure 3.8e

Figure 3.8: Time history of liquid and film motions on one-dimensional coordinates, blue ● region is liquid, red ● region is dry vapor, and yellow ● region is vapor covered by liquid films. For the small rectangles on the right end of figure 3.8e, ■ represents condenser regions and ■ represents heater regions

There is some disagreement in the OHP literature on the magnitude of sensible and latent heat contributions to the heat transfer. In this section we present our results for this issue. Figure 3.9 shows the sensible and latent heat comparison for four representative cases. Positive sensible heat is defined as the heat flow from the wall to liquid slugs. Negative sensible heat is defined as the heat flow from liquid slugs to the wall. Positive latent heat is defined as the evaporation heat flow from liquid films. Negative latent heat is defined as the condensation heat flow to liquid films. The internal heat flows from nucleate boiling and liquid slugs merging are neglected. It is shown from the simulations that the majority of the heat flow is in the form of latent heat in normal operating conditions. When dry-out occurs, both latent heat and sensible heat approach zero in Figure 3.9c. Quantitative comparisons can be made between the four cases in Figure 3.9 by defining average absolute sensible and latent heat values. The average absolute sensible heat is the time-averaged absolute value of the blue and red curves (averaged both in time and between two those two lines). Similarly, the average latent heat averages the green and lavender lines. The results are shown in Table 3.1. It can be seen that the average latent heat values are comparable across all four cases. The average sensible values are similar for three cases but for the OHP1 large heater at 40W, the sensible heat value is about half the others. This is due to a smaller temperature difference in this case, reflected in a larger thermal conductance in Figure 3.7 The sensible heat corresponds to the heat transfer between the wall and the liquid slug (since sensible heat transfer between the wall and vapor is neglected). For latent heat and sensible heat at lower power levels, the results are similar, but everything scaled less. And the OHP2 large heater case does not have dryout at lower power levels. The sensible and latent heat comparison for OHPs at a lower power level (20W) can be found at supplementary material.

OHP	heater size	power [W]	average latent heat [W]	average sensible heat [W]
1	large	40	31.32	3.05
1	small	40	27.30	6.20
2	large	40	25.32 (averaged until 200 s)	5.85
2	small	40	29.56	6.10
1	large	20	15.97	1.51
1	small	20	15.18	2.31
2	large	20	13.76	2.92
2	small	20	15.48	2.49

Table 3.1: The average latent heat and average sensible heat comparisons

Figure 3.9 and Table 3.1 show that the OHP1 larger heater configuration is unique. It has a much larger thermal conductance compared with other three configurations. It also has a smoother latent heat curve and a smaller percentage of sensible heat. This implies that there are more percentage of vapor that is covered by liquid films, which can also be verified visually from Figure 3.8. The correlation between more liquid films and a higher thermal conductance can guide the designing of an OHP, such as by having a configuration that can trigger more liquid slug motions.

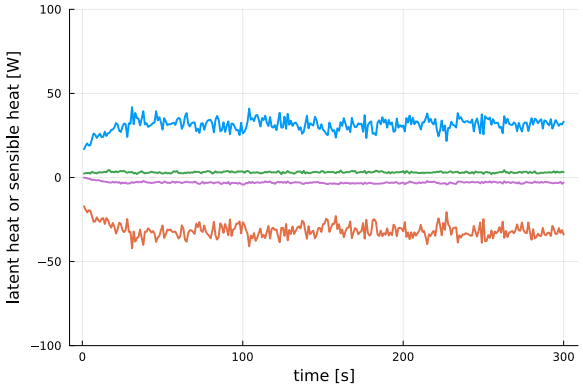

(a) OHP1 large heater 40 W

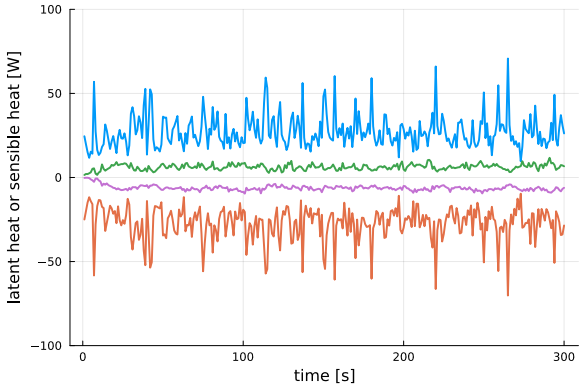

(b) OHP1 small heater 40 W

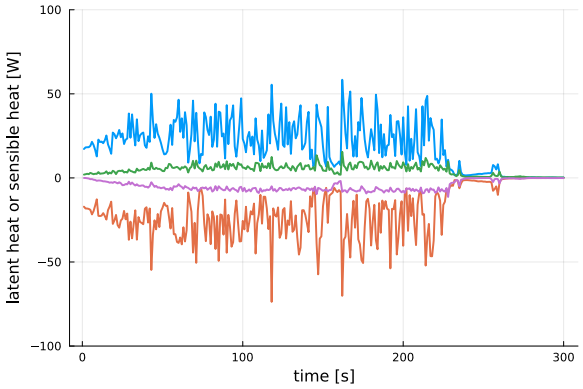

(c) OHP2 large heater 40 W

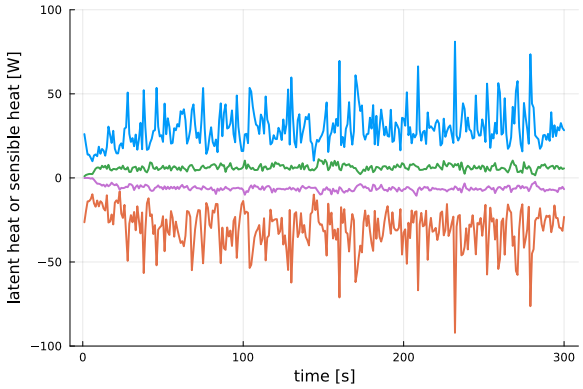

(d) OHP2 small heater 40 W

Figure 3.9: Latent heat and sensible heat comparisons, — is the positive latent heat, — is the negative latent heat, — is the positive sensible heat, and — is the negative sensible heat

CHAPTER 4

Further exploring of the validated OHP model

4.1 Comparison for ground-tested OHPs

In this chapter, we will compare simulations results with two ground-tested configurations. The first case is a horizontal OHP and the second case includes gravity effect and can be gravity-assisted. The purpose of this chapter is to show the versatility of the model when dealing with unknown configurations. Apart from the effective heat transfer coefficient between the condenser and the plate, all other physical parameters are the same as the previous chapter. The condenser's effective heat transfer coefficient is fixed compared with the on-orbit test. In other words, the condenser has a larger effective heat transfer coefficient to compensate a reduced condenser area.

Also noted that in this section, the above mentioned immersed boundary method is extended to enforce adiabatic boundary conditions on the edge of the metal plate. It thus enables using an arbitrary OHP shape with prescribed boundary condition and thus greatly enhanced the capabilities of the current simulation model. The geometry used in the below simulation is a 2 inches $\times$ 6 inches rectangular metal plate.

4.1.1 Large heater horizontal OHP comparison

This section shows a ground-tested OHP placed horizontally with a similar OHP channel geometry as the on-orbit large heater OHP1 in the last chapter. The working fluid is still butane. The purpose of this section is to verify how much different the ground tested OHP is compared with the on-orbit OHP. Their layouts have slight differences, as can be seen in Figure 4.1. There is only one heater

in the middle of the ground-tested OHP, with the same heating area but no gap in the middle. As for the condenser, the overlapping distance is only 15 mm, much shorter than the distance used in previous simulations (25.4mm).

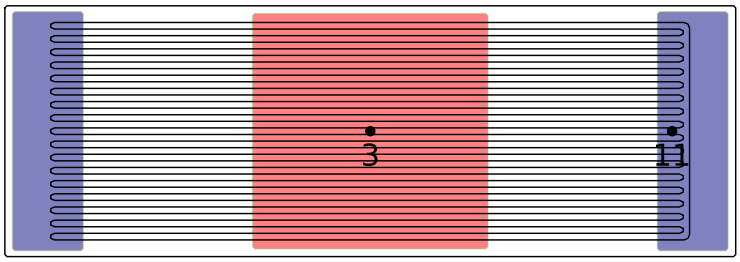

Figure 4.1: Dimensions and layouts of serpentine channels (black), evaporators (red), and condensers (blue) of the large heater ground-tested OHP

Figure 4.2 presents the temperature difference for the new OHP. Refering to Figure 3.3, the new OHP has a lower temperature difference (3.81 K) [Won24] compared with the OHP1 large heater on-orbit case (5.80 K) [DWT22]. In Figure 4.2, the model is seen to under-predict the thermal conductance (8.00 K). The discrepancy between the ground test simulations and experiment can result from OHP conditions such as a different charge ratio, an slightly misplaced internal channel geometry, and slightly misplaced sensor locations. A more comprehensive study of why the ground test case has better thermal conductance is worthwhile as future work. Here we explore these four possibilities that may be different in the ground-tested cases: the effect of charge ratios and effective heat transfer coefficients, the effect of channel length under the condenser, and the sensor location near the condenser.

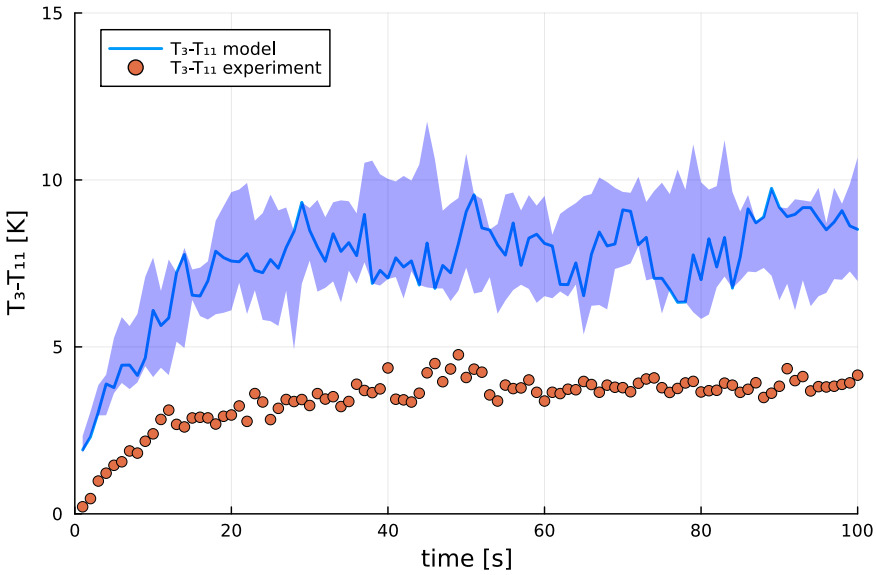

Figure 4.2: Temperature difference comparison between simulation and ground test at 40W heater

4.1.1.1 The effects of charge ratio and condenser effective heat transfer coefficient

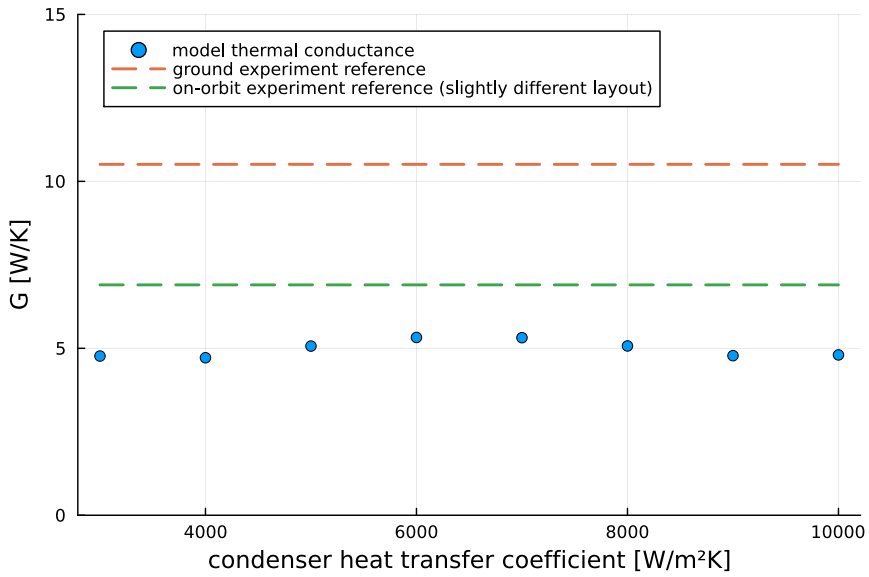

Figure 4.3: Thermal conductance for different condenser effective heat transfer coefficients. The reference value for on-orbit experiments is ASETS-II's OHP1 large heater at 40W [DWT22], the reference value for ground experiments is from Wong's experiments [Won24]

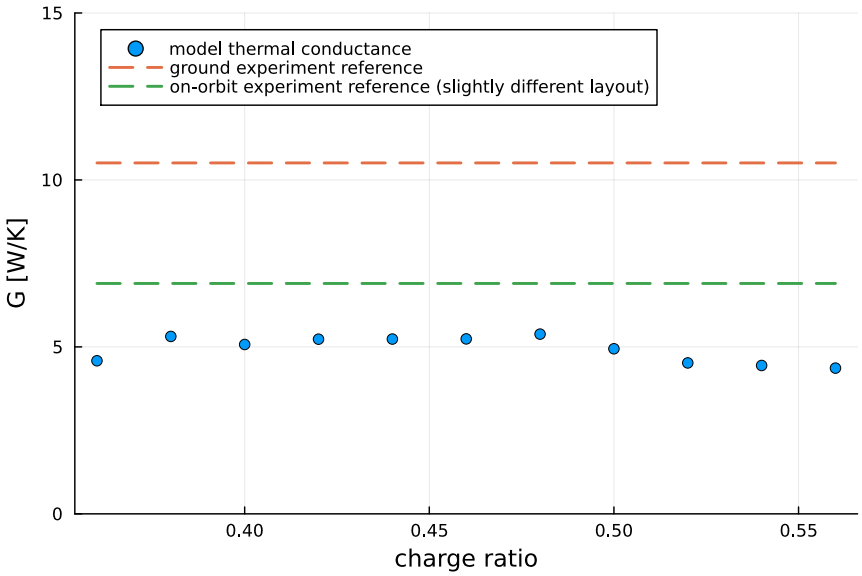

Figure 4.4: Thermal conductance for different charge ratios. The reference value for on-orbit experiments is ASETS-II's OHP1 large heater at 40W [DWT22], the reference value for ground experiments is from Wong's experiments [Won24]

Figure 4.3 shows the effect of condenser effective heat transfer coefficients on the thermal conductance, it shows little variation but cannot compensate for the difference between the simulation and the ground test data. Figure 4.4 shows the effect of charge ratios on the difference between the simulation and the ground test data. These two parameters are not showing evident influence on the thermal conductance.

4.1.1.2 The effects of internal channel geometry and sensor locations

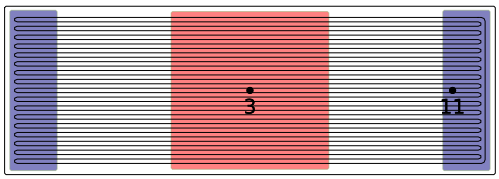

(a) Dimensions and layouts of the ground-tested OHP with an elongated channel

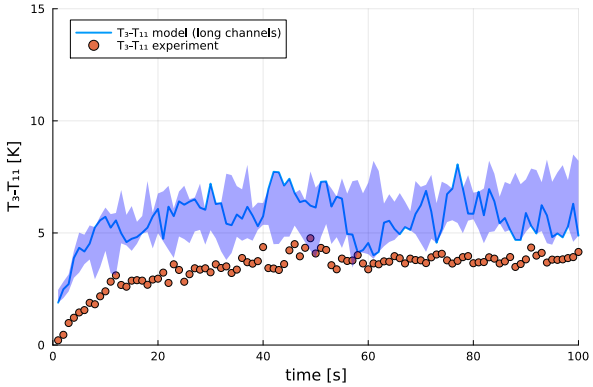

(b) Temperature difference comparison between simulation and ground test at 40W heater for a long channel OHP

Figure 4.5: Layouts and temperature difference for a long channel OHP

Figure 4.5b shows the temperature difference curve and comparison with experiments for an OHP with elongated inner channels. The layout of the elongated channels can be seen in Figure 4.5a. Because of the elongated channels, the contact area between the condenser and the channels is larger. The temperature difference significantly reduced from 5.648 K to 4.818 K in this case, showing that more area of channels under the condensers can help increase the overall thermal conductance. Figure 4.6b shows the temperature difference curve and comparison with experiments for an OHP with both elongated inner channels and a temperature sensor slightly misplaced to the left edge of the condenser. The location of the new sensor can be seen in Figure 4.6a. This set of result shows an even lower temperature difference compared with the case with only elongated inner channels. It shows that both having more overlap of channels and a sensor closer to the center of OHP helps to decrease the temperature difference.

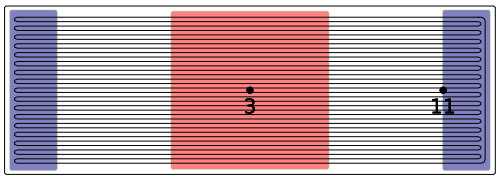

(a) Dimensions and layouts of the ground-tested OHP with an elongated channel with a sensor closer to the center

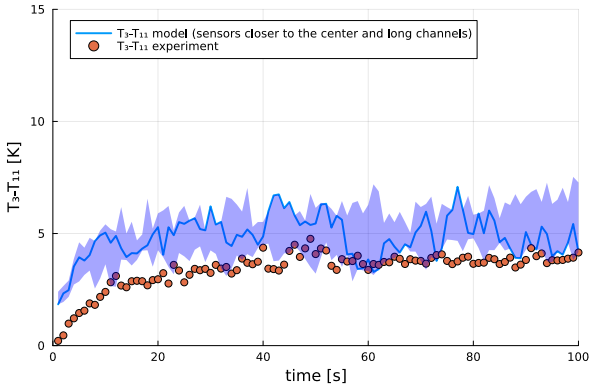

(b) Temperature difference comparison between simulation and ground test at 40W heater for a long channel OHP with a sensor closer to the center

Figure 4.6: Layouts and temperature difference for a long channel OHP with a sensor closer to the center

4.1.2 Gravity-assisted large heater OHPs

This section shows the thermal conductance result comparison with ground experiments for a large heater case. Figure 4.8 shows a new OHP configuration of a ground test, with a large heater of size (25mm x 50mm). and a condenser of size (15mm x 51mm). Keep noted that compared with the micro-gravity configurations, this OHP has a smaller condenser. This is a "gravity-assisted" case, it means when there is a positive inclination angle, the condenser side is tilted upward, see Figure 4.7. Then gravity can be used to resist the trend for liquid accumulating in the condenser region to delay the occurrence of dry-out.

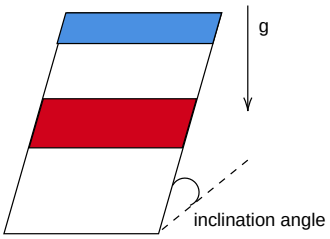

Figure 4.7: The OHP with a positive inclination angle

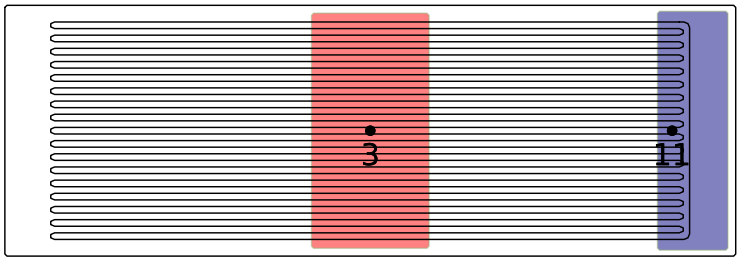

Figure 4.8: Dimensions and layouts of serpentine channels (black), evaporators (red), and condensers (blue) of the large heater ground-tested OHP

4.1.2.1 Different power levels

In this section, 16 cases are shown with four different inclination angles (0 °, 30°, 60°, and 90°) and four power levels (50 W, 60 W, 70W, and 80W).

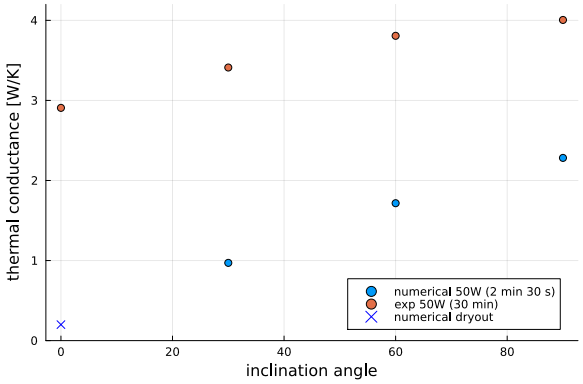

(a) Gravity-assisted 50W heater

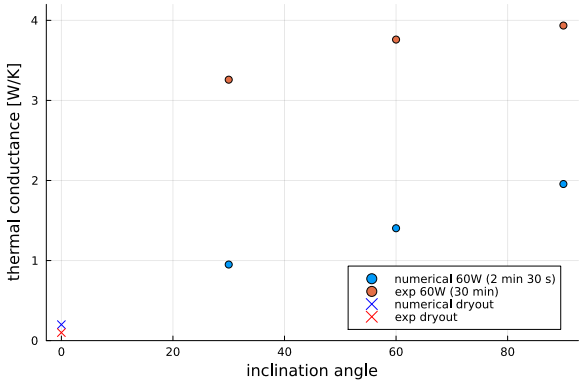

(b) Gravity-assisted 60W heater

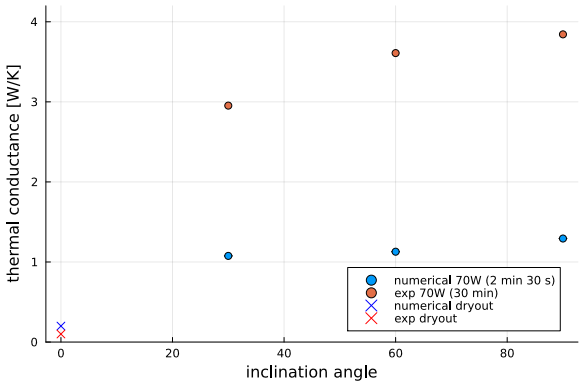

(c) Gravity-assisted 70W heater

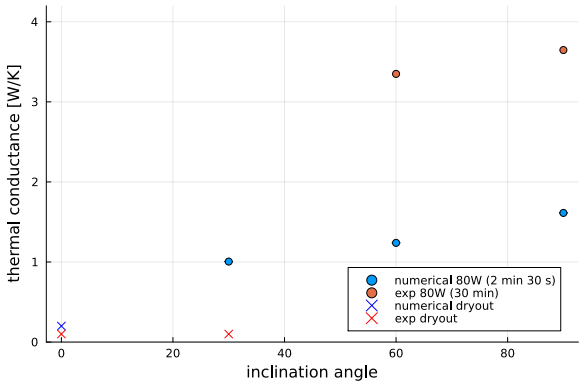

(d) Gravity-assisted 80W heater

Figure 4.9: Averaged thermal conductance comparison, red circles ● are experimental thermal conductance, and blue squares ■ are time-averaged numerical thermal conductance.

From Figure 4.9, we can see that for the same power level, an increase in inclination angle will result in an increase in the thermal conductance, and we can also find that for gravity-assisted configurations, dryout is less likely to happen at a higher inclination angle and a lower power. These figures show that the simulation results have good agreement with experimental data trends albeit still have roughly half the thermal conductance, using the same parameter set adjusted for the microgravity cases.

4.1.2.2 Different inclination angles

Another two figures are shown below, demonstrating the same results as Figure 4.9. The main purpose of Figure 4.10 is to show the influence of heater power on thermal conductance. It shows that with an increase in heater power, both the simulation and the experiment show a slight decrease in thermal performance when power is lower than 80W. For simulations, the conductance increased at 80W.

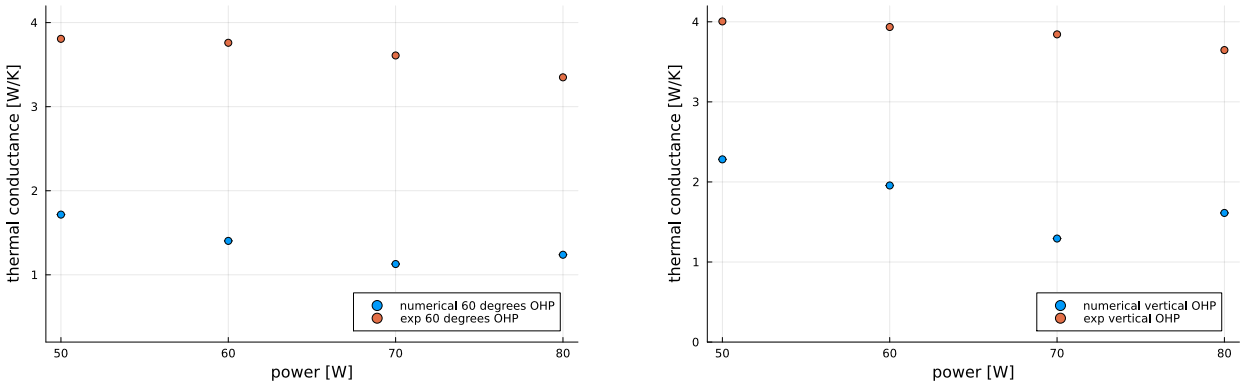

(a) Gravity-assisted 60 degrees

(b) Gravity-assisted 90 degrees

Figure 4.10: Averaged thermal conductance comparison, red circles ● are experimental thermal conductance, and blue squares ■ are time-averaged numerical thermal conductance.

4.2 Details of a single nucleate boiling event

This numerical model enables studying the effect of a single nucleate boiling event, by artificially setting one active nucleate boiling station. This will provide more knowledge on how boiling affects the system and how to design a better OHP. Figure 4.11 shows the layout of a simple three-turn OHP in a 2in x 6in metal plate with only one nucleation site under the heater. The heater's size is 50mm × 50mm. Each condenser's size is 30mm × 51mm.

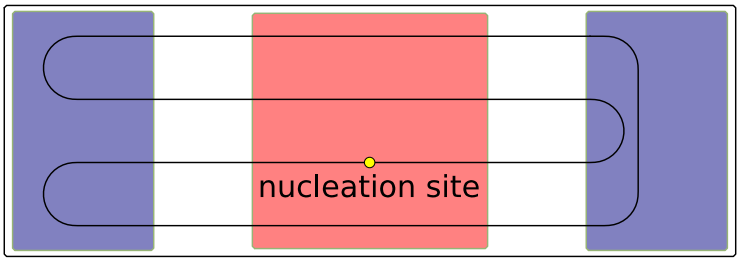

Figure 4.11: Layouts of serpentine channels (black), evaporators (red), and condensers (blue) of an OHP with only one nucleation site

Figure 4.12 shows the snapshots of the boiling event. At 0.21 s, the boiling hasn't occurred and the liquid slug is static. At 0.24 s, a small vapor bubble is generated and heated. From the snapshots at 0.6 s and 1.2 s, one can observe that the liquids slugs are being pushed by the pressure difference created by the new vapor bubble. The liquid slugs are depositing liquid films that are evaporated, this evaporation will increase the mass of the new vapor bubble. More details on the pressure and mass evolution can be seen in Figure 4.13.

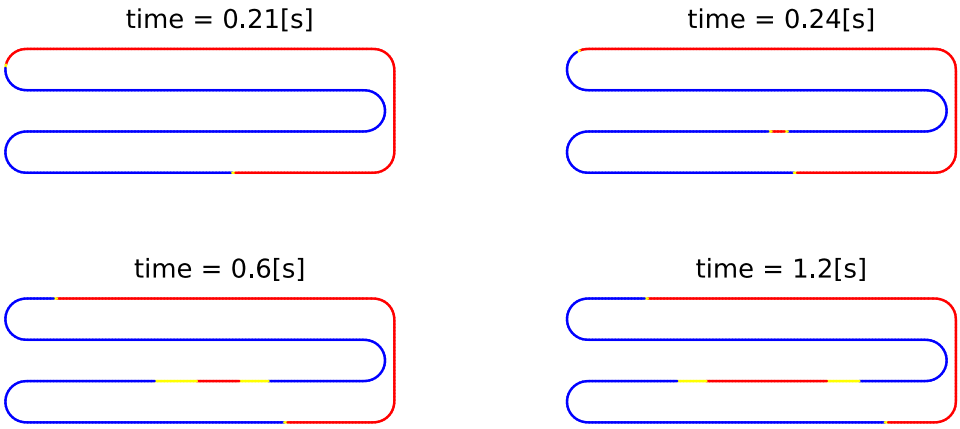

Figure 4.12: Snapshots for the OHP with only one nucleate boiling site, blue • region is liquid, red • region is dry vapor, and yellow • region is vapor covered by liquid films

Figure 4.13 shows the evolution of the pressure at the nucleation site and the mass of the vapor bubble over time. It can be seen that after a new bubble forms because of nucleate boiling, the vapor mass increases smoothly. When the liquid slugs are pushed out of the evaporator zone, the slope of vapor mass decreased and the pressure reaches maximum. However, the high pressure at nucleation site caused by this new bubble causes a vibration at a high frequency compared with the macro liquid slug oscillations observed in the previous simulations. This vibration caused by boiling quickly dampens down and thus a ringdown pressure curve is observed. The frequency of this ringdown depends not only the thermodynamics properties, but also the liquid slugs' lengths. But this ringdown does not have a large effect on the heat transfer afterwards. After the ringdown, the bubble further expands because of thermodynamics. This shows that when building a more reduced-order model of thermal performance, we can neglect the ringdown portion of the physics.

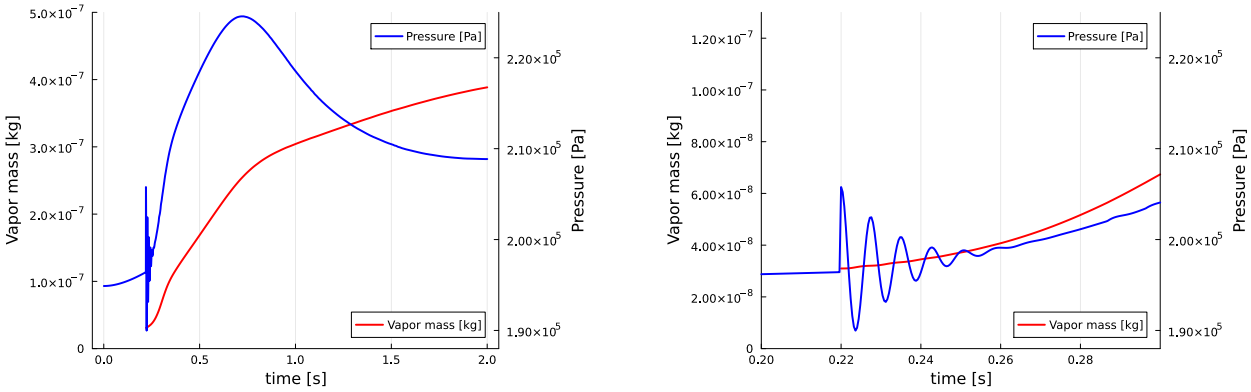

(a) the ringdown and longer-term effect of boiling

(b) closer look at the instant after boiling

Figure 4.13: The pressure and mass variation of the new vapor bubble

In this chapter, we compared the simulation with ground-tested experiments, the first comparison case is a horizontal OHP. The difference can be mitigated by having a longer channel length under the condensers and a temperature sensor closer to the middle of an OHP. The effect of charge ratio and condenser effective heat transfer coefficient are negligible. The second comparison is for an OHP with different inclination angle and heater power levels, despite the difference in values, the model predicts the trends well. In the future it is important to fully understand the reason for the difference between the ground-tested OHP and the simulation result.

CHAPTER 5

Data-assimilation of OHPs

When trying to build a numerical model of an OHP, some parameters that are hard to measure experimentally have to be assumed and further adjusted when comparing with experiments. These parameters stands for various phenomena such as the inertia-thickening effect, the condenser's heat transfer coefficient when it contacts the OHP, and the cavities' size of the micro-channels. They noticeably affect the result, thus it is possible to infer them from the simulation's comparison with experiments. Though in real applications, these parameters are manually turned, this chapter shows the feasibility of performing data-assimilation with OHP models. The first section starts with a very low-dimensional simplified U-turn OHP model [ZFS02] and uses the ensemble Kalman Filter to infer key parameters, including the wall heat transfer coefficient. The second section uses the complete OHP model and Markov chain Monte Carlo method to infer multiple possible parameters without assuming Gaussian uncertainty.

5.1 The ensemble Kalman Filter

In this chapter we introduce the formulation of the ensemble Kalman Filter (EnKF) and its application to a "toy" problem. EnKF is an approach of data-assimilation that can deal with non-linearity and high-dimensional systems. Before digging into EnKF, it is helpful to introduce its predecessor, the Kalman Filter (KF) first, and then some upgraded versions.

5.1.1 Kalman Filter

The discrete KF is firstly introduced by R.E. Kalman in 1960 [Kal60]. It is a recursive filter and ideal for real-time running because only the estimated state and covariance in the last step is needed. KF can provide optimal estimations if the initial state is Gaussian and the state transition matrix is linear, and the errors are uncorrelated Gaussian white noise. This can be derived by using the Bayes' rule to propagate conditional mean and variance for a Gauss-Markov process. But KF can also be derived by Orthogonal Projection Lemma, the way Kalman did [Kal60], where the measurement noise can be relaxed to be non-Gaussian. In this way, KF can still give the minimum-variance estimation. But in this paper, we assume Gaussian noise for simplicity.

For a dynamics system:

$$\begin{aligned} \boldsymbol{x}_{k+1} &= \boldsymbol{\Phi}_k \boldsymbol{x}_k + \boldsymbol{w}_k \\ \boldsymbol{z}_k &= \boldsymbol{H}_k \boldsymbol{x}_k + \boldsymbol{v}_k, \end{aligned} \tag{5.1}$$

where $\boldsymbol{x}_0 \sim \mathrm{N}\left(\bar{\boldsymbol{x}}_0, \boldsymbol{M}_0\right)$, $\boldsymbol{\Phi}_k$ is the state transition matrix at step k, and $\boldsymbol{H}_k$ is a projection from the state $\boldsymbol{x}_k$ to the measurement $\boldsymbol{z}_k$. $\boldsymbol{w}_k$ and $\boldsymbol{v}_k$ are additive process and measurement disturbances at step k with the properties:

$$\begin{aligned} \boldsymbol{w}_k &\sim \mathrm{N}\left(0, \boldsymbol{W}_k\right) \\ \boldsymbol{v}_k &\sim \mathrm{N}\left(0, \boldsymbol{V}_k\right) \end{aligned} \tag{5.2}$$

.

At the k_{th} time step, KF has two steps: the forecast (a priori) step and the analysis (a posteriori) step. In the forecast step, the state mean and state covariance from the last time step is updated:

$$\begin{aligned} \bar{\boldsymbol{x}}_k &= \boldsymbol{\Phi}_{k-1} \hat{\boldsymbol{x}}_{k-1} \\ \boldsymbol{M}_k &= \boldsymbol{\Phi}_{k-1} \boldsymbol{P}_{k-1} \boldsymbol{\Phi}_{k-1}^{\top} + \boldsymbol{W}_{k-1}. \end{aligned} \tag{5.3}$$

After getting $\boldsymbol{M}_k$ and $\bar{\boldsymbol{x}}_k$, in the analysis step, the a posteriori mean state is then estimated. And the a posteriori state covariance can also be derived.

$$\begin{aligned}\hat{\boldsymbol{x}}_k &= \bar{\boldsymbol{x}}_k + \boldsymbol{K}_k \left(\boldsymbol{z}_k - \boldsymbol{H}_k \bar{\boldsymbol{x}}_k\right). \\ \boldsymbol{P}_k &= \left(\boldsymbol{M}_k^{-1} + \boldsymbol{H}_k^\top \boldsymbol{V}_k^{-1} \boldsymbol{H}_k\right)^{-1}.\end{aligned} \tag{5.4}$$

$\left(\boldsymbol{z}_k - \boldsymbol{H}_k \bar{\boldsymbol{x}}_k\right)$ is also called residual. $\boldsymbol{K}_k$ is the Kalman gain, and $\boldsymbol{K}_k$ can be derived by:

$$\boldsymbol{K}_k = \boldsymbol{M}_k \boldsymbol{H}_k^\top \left(\boldsymbol{H}_k \boldsymbol{M}_k \boldsymbol{H}_k^\top + \boldsymbol{V}_k\right)^{-1}. \tag{5.5}$$

Equations 5.3, 5.4, and 5.5 constitute the basic formulations of the Kalman Filter.

However, in real life the dynamical systems, such as the thermofluid systems, are non-linear. This hinders the original linear KF's applicability. Thus non-linear extensions of KF are needed to deal with the non-linear systems.

5.1.2 Ensemble Kalman Filter

The ensemble Kalman Filter (EnKF) is firstly introduced by Evensen [Eve94]. It is a Monte Carlo version of KF. Instead of deriving the mean and covariance of the Gaussian random variables explicitly, it uses N ensemble members. Each ensemble member is a state vector initialized randomly at the beginning. They are directly propagated by the non-linear dynamics or observations. And the mean and covariance is then evaluated by the propagated ensemble members. The formulations are shown below. Note that $\boldsymbol{x}_{j,k}$ means the j_{th} ensemble member at time step k.

It also has the prediction step and the analysis step. In the prediction step:

$$\bar{\boldsymbol{x}}_k^j = \boldsymbol{f}_k \left(\hat{\boldsymbol{x}}_{k-1}^j\right) \tag{5.6}$$

Note that the effect of $\boldsymbol{w}_{j,k}$ will be explicitly introduced in the next section. Then the ensemble a priori mean and covariance can be derived. For convenience, the subscript k is omitted for the remainder of this section.

$$\bar{\boldsymbol{x}}_{\text{avg}} = \frac{1}{N} \sum_{j=1}^{N} \bar{\boldsymbol{x}}^j \tag{5.7}$$

Before advancement to the analysis step, a covariance inflation step is needed. For a small ensemble size, it will result in an underestimated error covariance [Van99]. When measurement covariance is fixed, this will result in throwing out the measurement data eventually. To fix this issue, an empirical multiplicative covariance inflation parameter β is introduced:

$$\bar{\boldsymbol{x}}^j := \bar{\boldsymbol{x}}_{\text{avg}} + \beta \left(\bar{\boldsymbol{x}}^j - \bar{\boldsymbol{x}}_{\text{avg}} \right) + \boldsymbol{\alpha}^j \tag{5.8}$$

$\boldsymbol{\beta}$ is a scalar larger than 1 but close to 1. α is Gaussian white noise vector representing the error of the model and provides a lower bound of the error covariance.

After the covariance inflation, the a priori error covariance is finally derived:

$$\bar{\boldsymbol{M}} = \frac{1}{N-1} \sum_{j=1}^{N} \left(\bar{\boldsymbol{x}}^j - \bar{\boldsymbol{x}}_{\text{avg}} \right) \left(\bar{\boldsymbol{x}}^j - \bar{\boldsymbol{x}}_{\text{avg}} \right)^{\top}. \tag{5.9}$$

In the analysis step, firstly, the Kalman gain (K) can be derived by:

$$\boldsymbol{K} = \bar{\boldsymbol{M}} \boldsymbol{H}^{\top} \left(\boldsymbol{H} \bar{\boldsymbol{M}} \boldsymbol{H}^{\top} + \boldsymbol{V} \right)^{-1}, \tag{5.10}$$

where $\boldsymbol{H}$ is the tangent linear of the observation function. And $\boldsymbol{V}$ is the measurement error covariance. After getting $\boldsymbol{K}$, the a posteriori $\hat{\boldsymbol{x}}$ can be derived:

$$\hat{\boldsymbol{x}}^j := \bar{\boldsymbol{x}}^j + \boldsymbol{K} \left(\boldsymbol{z} - \boldsymbol{h}(\bar{\boldsymbol{x}}^j) + \boldsymbol{v}^j \right) \tag{5.11}$$

$\boldsymbol{z}$ is the measurement. Note that the same $\boldsymbol{z}$ is used for all ensemble members, thus a random white noise $\boldsymbol{v}^j$ is needed with covariance $\boldsymbol{V}$ to reflect the randomness of measurements and avoid spurious correlations [BLE98].

5.1.3 Implementing EnKF for U-tube parameter estimation

5.1.3.1 Numerical "truth" results for measurements

To validate our EnKF, we implement it into the above U-tube dynamics model. But the model is with a few modifications here. Instead of having a constant H_{e}, we use an impulsive changing H_{e} to represent there is a sudden change of heat flux:

$$H_{\mathrm{e}} = \begin{cases} 3000 & 0 \leq \mathcal{T} \leq 0.05 \\ 30000 & 0.05 < \mathcal{T} \leq 0.1 \end{cases} . \tag{5.12}$$

The results under the new definition of H_{e} at time step k is named as $\boldsymbol{x}_{real,k}$.

5.1.3.2 EnKF prediction step

We use 50 ensemble members, thus $N = 50$. In the EnKF scheme, H_{e} is now appended as a part of the state vector:

$$\boldsymbol{x}_{\mathrm{EnKF}} = \begin{bmatrix} Z_{\mathrm{p},1} & Z_{\mathrm{p},2} & \frac{\mathrm{d}Z_{\mathrm{p},1}}{\mathrm{d}\mathcal{T}} & \frac{\mathrm{d}Z_{\mathrm{p},2}}{\mathrm{d}\mathcal{T}} & M_{\mathrm{v},1} & M_{\mathrm{v},2} & H_{\mathrm{e}} \end{bmatrix}^T = \begin{bmatrix} \boldsymbol{x} & H_{\mathrm{e}} \end{bmatrix}^T \tag{5.13}$$

Thus we can estimate H_{e} when estimating $\boldsymbol{x}_{\mathrm{EnKF}}$. For EnKF, it is unknown that H_{e} is not a constant anymore. So the predictor's equation still assumes a constant H_{e} all the time and $\boldsymbol{f}_{\mathrm{EnKF}}(\boldsymbol{x}_{\mathrm{EnKF}})$ is

$$\frac{\mathrm{d}}{\mathrm{d}\mathcal{T}} \begin{bmatrix} \boldsymbol{x} \\ H_{\mathrm{e}} \end{bmatrix} = \begin{bmatrix} \boldsymbol{f}(\boldsymbol{x}) \\ 0 \end{bmatrix} = \boldsymbol{f}_{\mathrm{EnKF}}(\boldsymbol{x}_{\mathrm{EnKF}}). \tag{5.14}$$

By discretizing, $\boldsymbol{f}_{\mathrm{EnKF}}(\boldsymbol{x}_{\mathrm{EnKF}})$ in explicit 4th-order Runge-kutta scheme, $\boldsymbol{f}_{\mathrm{EnKF},k}$ can be derived. And $\bar{\boldsymbol{x}}^j_{\mathrm{EnKF},k}$ can be derived from $\hat{\boldsymbol{x}}^j_{\mathrm{EnKF},k-1}$.

The initial condition of the EnKF predictor is

$$
\begin{cases}
Z_{\mathrm{p},1}^{j} \sim \mathrm{N}\left(1.0, 1\times 10^{0}\right) \\
Z_{\mathrm{p},2}^{j} \sim \mathrm{N}\left(3.0, 1\times 10^{0}\right) \\
(\frac{\mathrm{d}Z_{\mathrm{p},1}}{\mathrm{d}t})^{j} \sim \mathrm{N}\left(0.0, 1\times 10^{4}\right) \\
(\frac{\mathrm{d}Z_{\mathrm{p},2}}{\mathrm{d}t})^{j} \sim \mathrm{N}\left(0.0, 1\times 10^{4}\right) \\
M_{\mathrm{v},1}^{j} \sim \mathrm{N}\left(1.0, 1\times 10^{0}\right) \\
M_{\mathrm{v},2}^{j} \sim \mathrm{N}\left(3.0, 1\times 10^{0}\right) \\
H_{\mathrm{e}}^{j} \sim \mathrm{N}\left(0.0, 1\times 10^{0}\right)
\end{cases} . \tag{5.15}
$$

5.1.3.3 EnKF analysis step

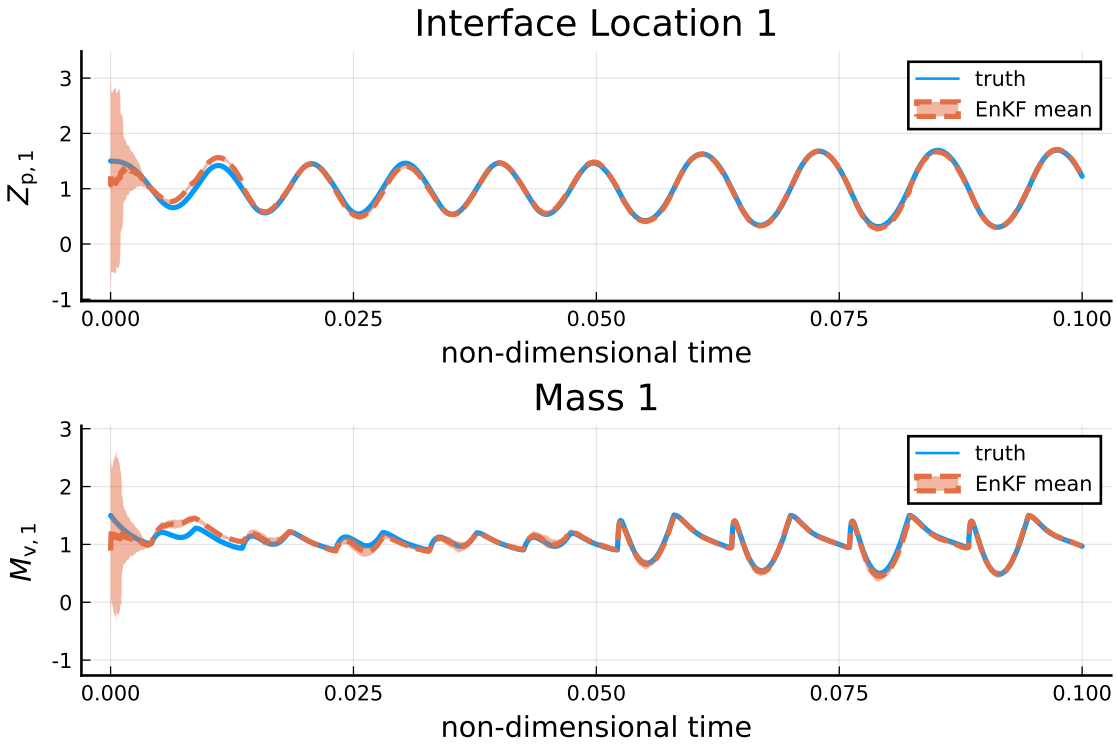

Figure 5.1: Non-dimensional $Z_{\mathrm{p},1}$ and $M_{\mathrm{v},1}$ reference and estimation

In this section, the subscript $_{\mathrm{EnKF},k}$ is omitted for convenience.

The time interval of measurements is 1×10^{-5} non-dimensional time, the same as the predictor

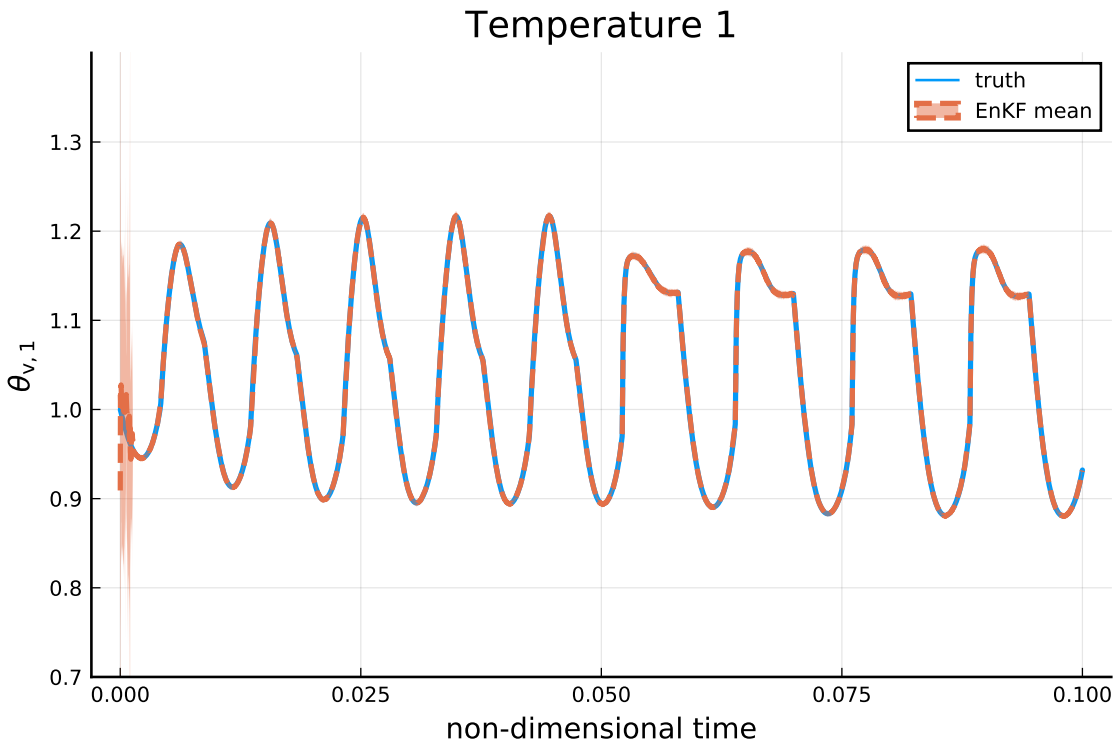

Figure 5.2: Non-dimensional $\theta_{v,1}$ reference and estimation

model. The multiplicative inflation $\beta = 1.001$.

The covariance matrix for additive inflation $\boldsymbol{\alpha}$ is

$$\boldsymbol{\mathcal{A}} = \begin{bmatrix} 1 \times 10^{-5} & & & & & & \\ & 1 \times 10^{-5} & & & & & \\ & & 1 \times 10^{0} & & & & \\ & & & 1 \times 10^{0} & & & \\ & & & & 1 \times 10^{-5} & & \\ & & & & & 1 \times 10^{-5} & \\ & & & & & & 1 \times 10^{7} \end{bmatrix}. \tag{5.16}$$

The measurement noise covariance matrix $\boldsymbol{V}$ is

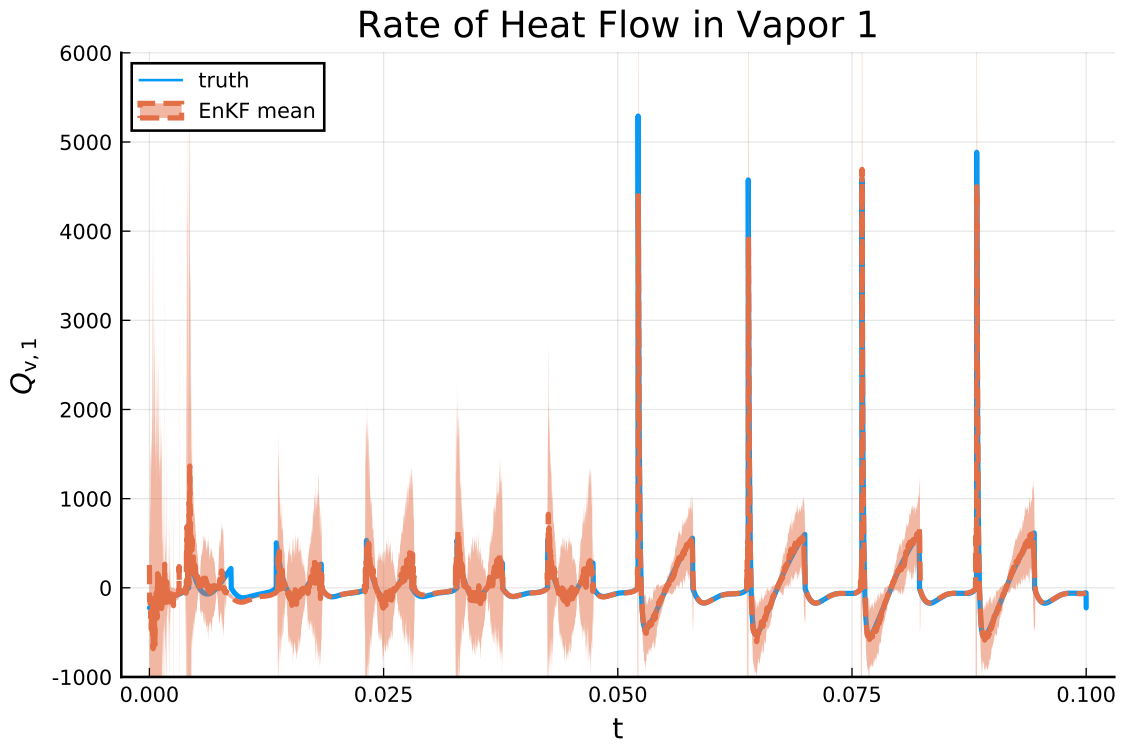

Figure 5.3: Non-dimensional phase change heat flow rate reference and estimation, $Q_{\mathrm{v},i} = \frac{\mathrm{d}M_{\mathrm{v},i}}{\mathrm{d}\mathcal{T}}$

$$\boldsymbol{V} = \begin{bmatrix} 1 \times 10^{-5} & \\ & 1 \times 10^{-5} \end{bmatrix}. \tag{5.17}$$

The measurement is the temperature in the two vapor slugs $\theta_{\mathrm{v},1}$ and $\theta_{\mathrm{v},2}$. It is a non-linear function of the state vector. Here we linearize it to get the Kalman gain by using an augmented state vector f_{aug}, as is proposed by Evensen [Eve09]. This can be thought as an implicit linearization.

If the predicted measurement is $\boldsymbol{h}(\boldsymbol{x}^j)$ for every ensemble member j , we can construct a new augmented state vector:

$$\boldsymbol{x}^j_{\mathrm{aug}} = \begin{bmatrix} \boldsymbol{x}^j \\ \boldsymbol{m}^j \end{bmatrix}, \tag{5.18}$$

where the measurement vector $\boldsymbol{m}^j$ is

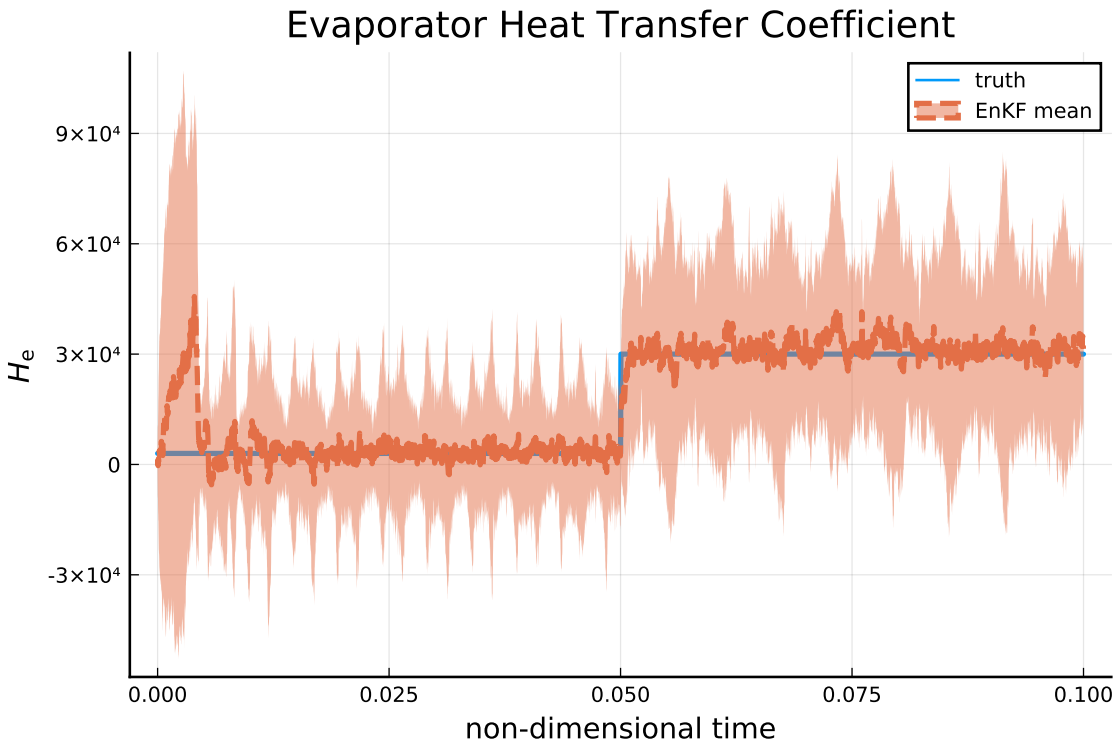

Figure 5.4: Non-dimensional evaporative heat transfer coefficient reference and estimation

$$\bar{\boldsymbol{m}}^j = \boldsymbol{h}(\bar{\boldsymbol{x}}^j) = \begin{bmatrix} \bar{\theta}^j_{\mathrm{v},1} \\ \bar{\theta}^j_{\mathrm{v},2} \end{bmatrix}. \tag{5.19}$$

Then a linear measurement matrix is obtained:

$$\boldsymbol{H} = \begin{bmatrix} \boldsymbol{0}^{7\times7} & \boldsymbol{0}^{7\times2} \\ \boldsymbol{0}^{2\times7} & \boldsymbol{I}^{2\times2} \end{bmatrix}. \tag{5.20}$$

Then, the mean and covariance of $\boldsymbol{m}$ are calculated:

$$\begin{aligned} \bar{\boldsymbol{m}}_{\mathrm{avg}} &= \tfrac{1}{N}\textstyle\sum_{j=1}^{N} \bar{\boldsymbol{m}}^j \\ \bar{\boldsymbol{\mathcal{M}}} &= \tfrac{1}{N-1}\textstyle\sum_{j=1}^{N} \left(\bar{\boldsymbol{m}}^j - \bar{\boldsymbol{m}}_{\mathrm{avg}}\right)\left(\bar{\boldsymbol{m}}^j - \bar{\boldsymbol{m}}_{\mathrm{avg}}\right)^{\mathrm{T}} \end{aligned}. \tag{5.21}$$

Also, the cross-covariance matrix between $\boldsymbol{x}^j$ and $\boldsymbol{m}^j$ can be also derived:

$$\bar{\boldsymbol{C}} = \frac{1}{N-1}\sum_{j=1}^{N}\left(\bar{\boldsymbol{x}}^{j} - \bar{\boldsymbol{x}}_{\text{avg}}\right)\left(\bar{\boldsymbol{m}}^{j} - \bar{\boldsymbol{m}}_{\text{avg}}\right)^{\mathrm{T}}. \tag{5.22}$$

Now, the a priori covariance matrix for the augmented state is:

$$\bar{\boldsymbol{M}}_{\text{aug}} = \begin{bmatrix} \bar{\boldsymbol{M}} & \bar{\boldsymbol{C}} \\ \bar{\boldsymbol{C}}^{\mathrm{T}} & \bar{\boldsymbol{\mathcal{M}}} \end{bmatrix}. \tag{5.23}$$

$\boldsymbol{M}$ is derived in the same way as equation.5.9.

Thus the Kalman gain ($\boldsymbol{K}_{\text{aug}}$) for the augmented state is

$$\begin{aligned} K_{\text{aug}} &= \bar{\boldsymbol{M}}_{\text{aug}}\boldsymbol{H}^{\mathrm{T}}\left(\boldsymbol{H}\bar{\boldsymbol{M}}_{\text{aug}}\boldsymbol{H}^{\mathrm{T}} + \boldsymbol{V}\right)^{-1} \\ &= \begin{bmatrix} \bar{\boldsymbol{C}}\left(\boldsymbol{V} + \bar{\boldsymbol{\mathcal{M}}}\right)^{-1} \\ \bar{\boldsymbol{\mathcal{M}}}\left(\boldsymbol{V} + \bar{\boldsymbol{\mathcal{M}}}\right)^{-1} \end{bmatrix} \end{aligned}. \tag{5.24}$$

Only the upper part is used to represent the actual Kalman gain (K) for the real system. The final analysis step with linearized measurement is then:

$$\hat{\boldsymbol{x}}^{j} := \bar{\boldsymbol{x}}^{j} + \bar{\boldsymbol{C}}\left(\boldsymbol{V} + \bar{\boldsymbol{\mathcal{M}}}\right)^{-1}\left(\boldsymbol{z} - \boldsymbol{h}(\boldsymbol{x}^{j}) + \boldsymbol{v}^{j}\right) \tag{5.25}$$

Then the a posteriori state is then propagated.

Figure 5.1 shows the estimation results and "truth" results for the first interface location $Z_{\text{p,1}}$ and the first vapor's mass $M_{\text{v,1}}$. Figure 5.2 shows the estimation results and "truth" results for the first first vapor's temperature $\theta_{\text{v,1}}$ that is taken measurements of. Figure 5.3 shows the phase change heat flow rate into the vapor 1. Figure 5.4 shows the evaporative heat transfer coefficient. As can be seen, after a while, the EnKF successfully estimates the flow states, especially the jump of H_{e} at time 0.05.

5.2 The Markov chain Monte Carlo method

One challenge of using an original EnKF method is that it assumes Gaussian noise for the state variables. This is not always the case. For a nonlinear problem, there can exist multiple possible parameters that can produce the same result. In this case, the probability density function can have multiple peaks. The Markov chain Monte Carlo (MCMC) method is a sampling method to get a desired probability distribution and often coupled with Bayes theorem. It only needs to know the relative probability between two samples and try to sample more on high-probability region.

Figure 5.5 shows the Metrapolis-Hastings method, which is the workhorse of MCMC method. In a Markov chain, the Metrapolis-Hastings method will propose a new sample based on the last sample and a proposal distribution (which is Gaussian as shown), then it will move to the new sample at a certain probability that makes it more likely to step to a sample that has a higher probability. The advantage of the Metrapolis-Hastings method is that it does not need to know the gradient data of the solver and thus it can couple with arbitrary solvers with no modifications.

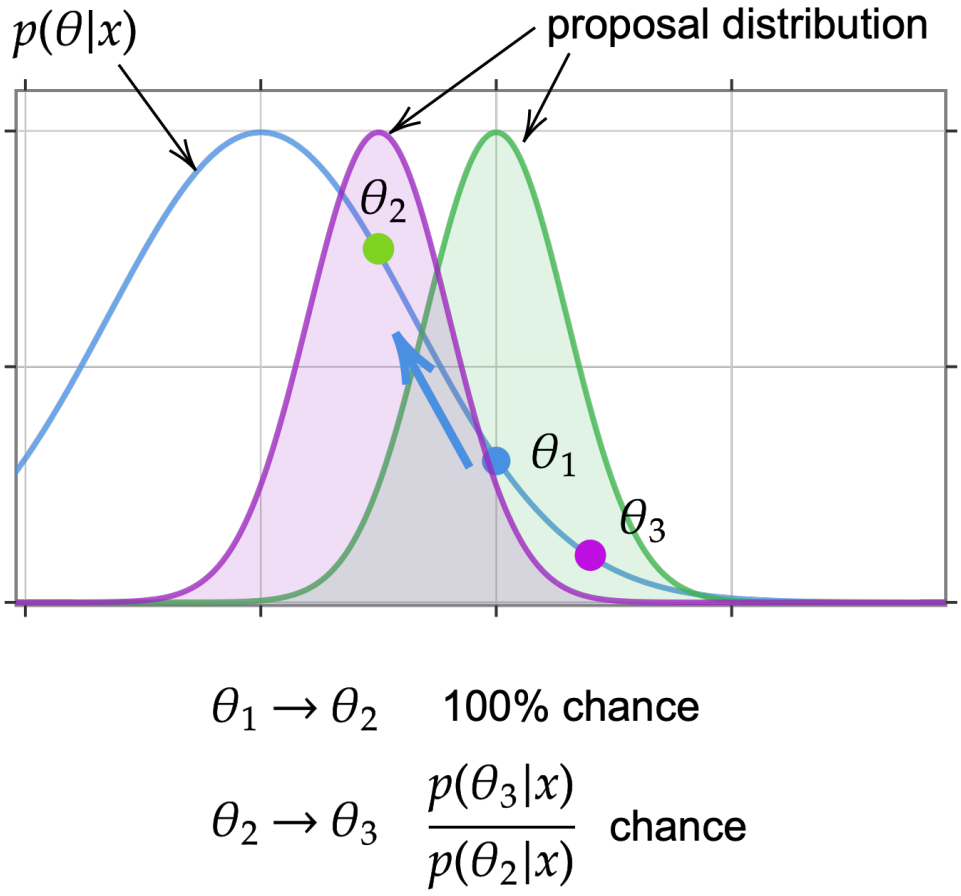

Figure 5.5: Schematic of Metrapolis-Hastings method

5.2.1 Demonstration of MCMC in a simple problem

To show how MCMC is working, we firstly deal with a simple heat conduction problem: inferring the plate thickness and condenser heat transfer coefficient from temperature measurements. In this task, as shown in Figure 5.6, an artificial temperature field with a Gaussian noise was generated using the solid module and no OHP is involved. And then MCMC is used to infer two parameters: one is the plate thickness, the other is the condenser's heat transfer coefficient.

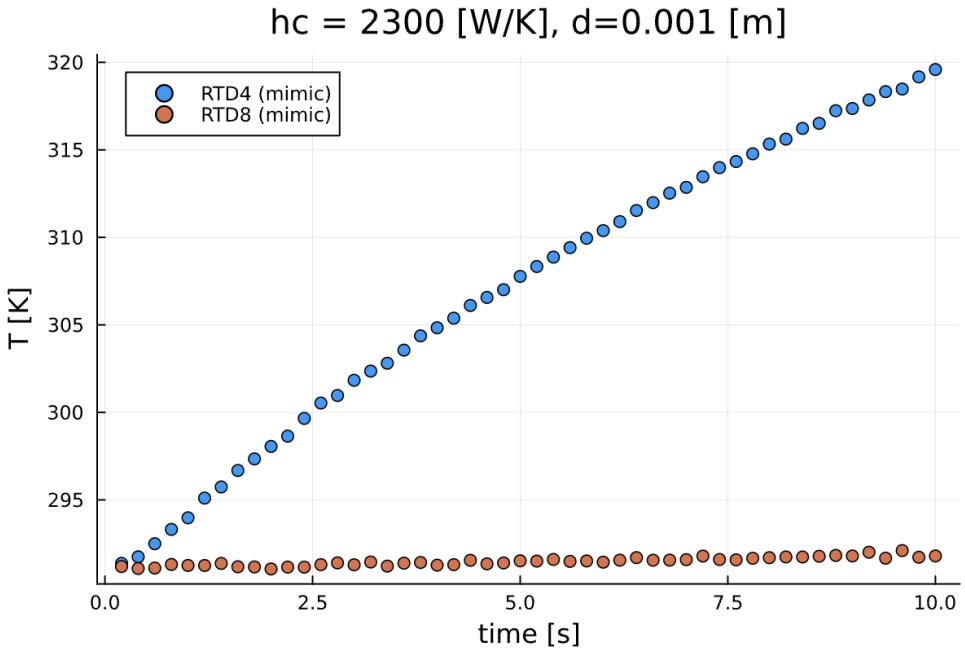

Figure 5.6: Temperature curve serving as "truth" data

It can be seen from Figure 5.7 that the plate thickness quickly converges to the actual value. Figure 5.8 shows that the condenser heat transfer coefficient converges slightly slower as this value is less observable than the plate thickness. But after 1000 steps, these two values stay stabilized and are close to the actual values.

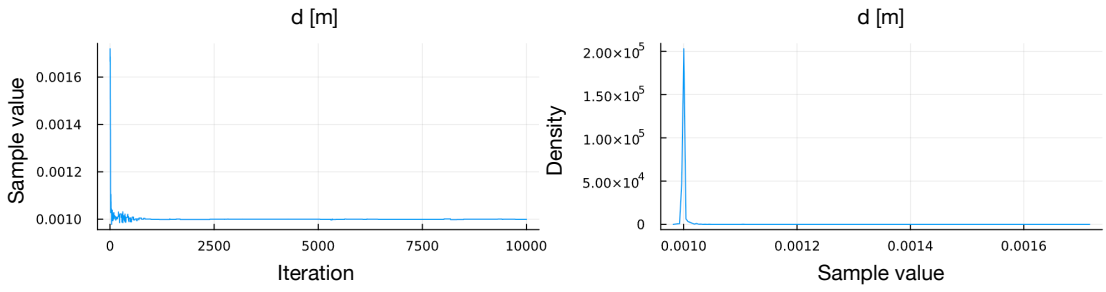

Figure 5.7: Iteration and probability of plate thickness d

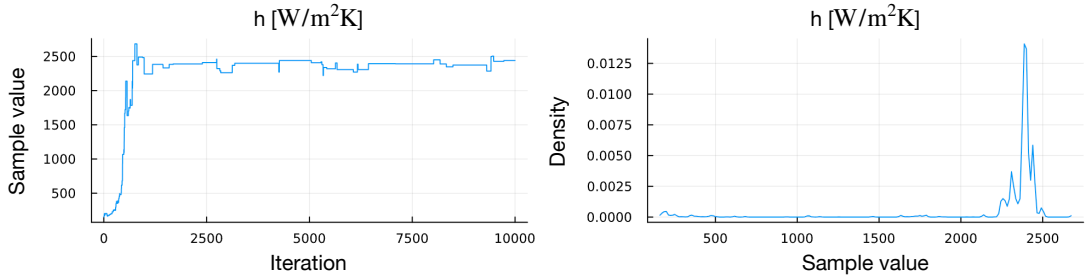

Figure 5.8: Iteration and probability of evaporator contact conductance per area h

Note that, unlike EnKF, each iteration of MCMC is a whole simulation. Thus MCMC can be very computationally demanding, especially when the forward simulation model is expensive to run. For this thermal conduction problem lasting 10 physical seconds, each simulation requires 100 time steps and 10000 iterations will take around 40 minutes to run on a Macbook Air with a M1 chip. But when dealing with a problem with an actual OHP, the simulation will be significantly slower and this will affect the performance of MCMC.

5.2.2 MCMC application to the coupled OHP model

In this section, we apply MCMC to our full OHP model to infer its film dynamics and condenser heat transfer coefficients. This is more challenging than pure conduction problems. Not only is the simulation much slower because of a smaller time step and the coupled OHP, but also the inertia-thickening factor that determines the film thickness can have a non-monotonic effect on the thermal performance. In other words, there may exist two possible inertia-thickening factors to produce the same temperature curves. In this case, MCMC shows its advantage of not assuming Gaussian parameter uncertainty. Due to the high requirement of computational power, only the experimental results for the first 2 seconds are used for data-assimilation, as shown in Figure 5.9.

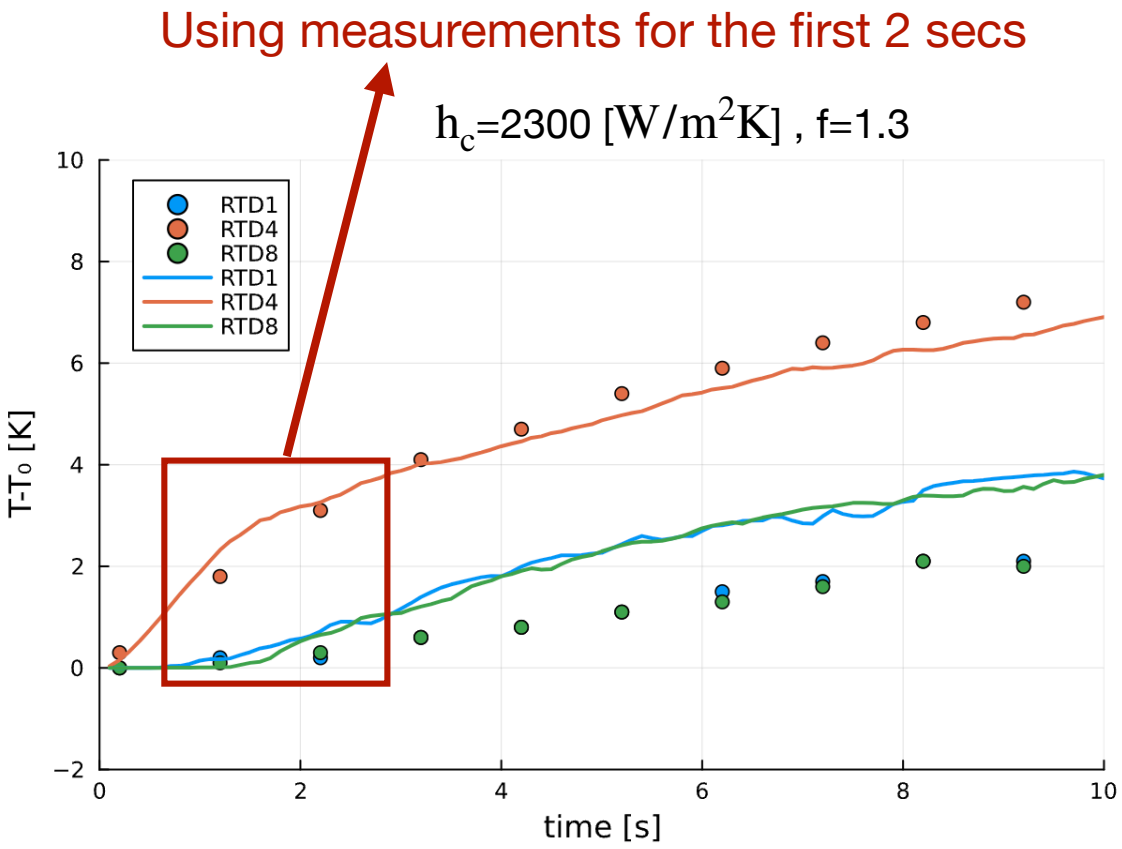

Figure 5.9: Temperature curve of simulation using current model and comparison with ASETS-II experiment OHP1 large heater 40W case represented by dots

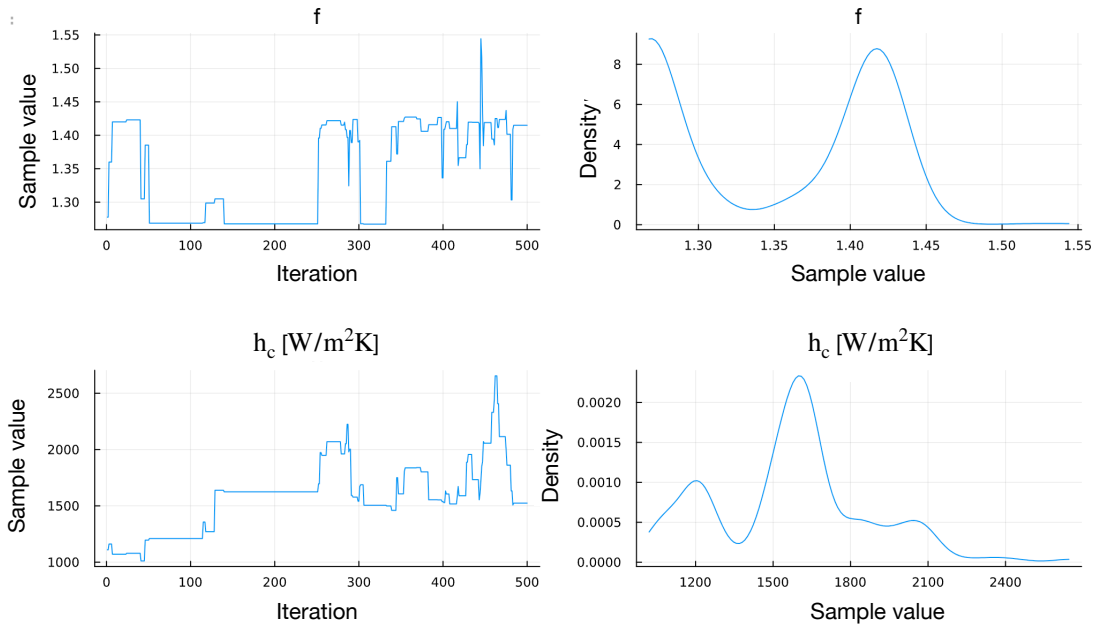

Figure 5.10: Iteration and probability of inertia-thickening factor f and condenser heat transfer coefficient h_c

Figure 5.10 shows the result of 500 iterations. We can notice that the inertia-thickening factor f switches between two values. And thus the probability density function shows two peaks. The heat transfer coefficient shows a most possible value of around 1600 W/m^{2}K, not far away from what the simulation used (2300 W/m^{2}K). These 500 Markov Chain iterations require 500 simulations in serial, which take a total of 12 hours of simulation time only for the first 2 seconds physical time. Although the number of iterations is low under typical standards of MCMC to "burn-in", it still shows inspiring results.

In this chapter, we explored two different techniques of data-assimilation, to infer parameters that are hard to measure. The EnKF method can estimate states with nonlinear dynamics with at a low computational cost. But the challenge of EnKF is that it assumes Gaussian uncertainties, which is not always a good assumption for an OHP. The MCMC method can estimate parameters with non-Gaussian uncertainty, but it has a high-computational cost because MCMC requires thousands of

iterations to converge, and each iteration is a whole simulation. In the future, when estimating the parameters of an OHP, these two challenges need to be resolved.

CHAPTER 6

Conclusion and Future Work

A model of oscillating heat pipes has been developed that captures the essential physics, including accounting for liquid films with time-varying length and thickness and conjugate heat transfer in the embedding plate. The immersed boundary method enables the solid module to solve this 2D conjugate heat transfer problem using a uniform Cartesian grid system, providing the model with novel flexibility for OHP, evaporator, and condenser geometries. The simulation shows good overall agreement with experiments, successfully predicting dryout in the OHP2 large heater 40 W case. To the authors' knowledge, this is the first prediction of experimentally-observed transition to dryout in OHP models. The simulation also shows the different oscillating features for large heater and small heater cases. In addition, it is shown that latent heat is the dominant contribution to heat transfer in these cases. This model aims to provide a data-assimilation framework for OHPs. All 16 cases were run using the same parameter set. This model, while containing adequate essential physics, is also very efficient to solve. A typical 300 s physical time simulation takes around 3 hours computational time on a Macbook Air laptop with M1 chip. The most updated code can be found at the url: `https://github.com/liyuxuan48/OscillatingHeatPipe.git`

This model was then also tested in gravity-assisted configurations, with the same fluids and solid parameters. Overall the model predicts the trend of thermal conductance with respect to inclination angle and power level well, with some error in conductance values. I explored several parameters that may affect the thermal performance. And also data-assimilation tools including EnKF and MCMC are used to estimate OHP parameters and estimate the prediction uncertainty both for Gaussian and non-Gaussian uncertainties.

In the future, there are still several questions to be answered:

1. How to physically understand the transition to dry-out is still an on-going issue. For example, it would be interesting to see this problem from a dynamical system point of view. When dry-out happens, this dynamics system reaches a fixed point. This system us deterministic once the initial liquid slugs and nucleation sites are known. Whether this transition is sensitive to the initial liquid slug distributions is still a question to be answered. In other words, if we tweak one liquid slug's initial location by a little bit, will this cause a much different dry-out result?

2. We only explored a specific type of OHP that have parallel channels filled with butane in a metal plate. More types of OHPs and more kinds of working fluids can be explored.

3. This current fluids modeling approach uses a lagrangian framework to track the interfaces and thus the time step during simulation is limited to avoid liquid slug overlapping. Can we instead use a continum model to allow a larger time step in simulations?

REFERENCES

[Aka90] Hisateru Akachi. "Structure of a heat pipe.", May 1 1990. US Patent 4,921,041.

[AMN22] Mauro Abela, Mauro Mameli, Vadim Nikolayev, and Sauro Filippeschi. "Experimental analysis and transient numerical simulation of a large diameter pulsating heat pipe in microgravity conditions." *International Journal of Heat and Mass Transfer*, **187**:122532, 2022.

[AQ00] Pascale Aussillous and David Quéré. "Quick deposition of a fluid on the wall of a tube." *Physics of fluids*, **12**(10):2367–2371, 2000.

[BLE98] Gerrit Burgers, Peter Jan van Leeuwen, and Geir Evensen. "Analysis scheme in the ensemble Kalman filter." *Monthly weather review*, **126**(6):1719–1724, 1998.

[BLK17] Joohan Bae, Sang Yong Lee, and Sung Jin Kim. "Numerical investigation of effect of film dynamics on fluid motion and thermal performance in pulsating heat pipes." *Energy Conversion and Management*, **151**:296–310, 2017.

[BWQ14] Ian H. Bell, Jorrit Wronski, Sylvain Quoilin, and Vincent Lemort. "Pure and Pseudo-pure Fluid Thermophysical Property Evaluation and the Open-Source Thermophysical Property Library CoolProp." *Industrial & Engineering Chemistry Research*, **53**(6):2498–2508, 2014.

[Chu77] Stuart W Churchill. "Friction-factor equation spans all fluid-flow regimes." 1977.

[CKK98] Lipeng Cao, J Peter Krusius, Matti A Korhonen, and Timothy S Fisher. "Transient thermal management of portable electronics using heat storage and dynamic power dissipation control." *IEEE Transactions on Components, Packaging, and Manufacturing Technology: Part A*, **21**(1):113–123, 1998.

[CKK15] Aditya Cherukumudi, Evert Klaseboer, Saif A Khan, and Rogerio Manica. "Prediction of the shape and pressure drop of Taylor bubbles in circular tubes." *Microfluidics and Nanofluidics*, **19**:1221–1233, 2015.

[DNA17] Takurou Daimaru, Hiroki Nagai, Makiko Ando, Kosuke Tanaka, Atsushi Okamoto, and Hiroyuki Sugita. "Comparison between numerical simulation and on-orbit experiment of oscillating heat pipes." *International Journal of Heat and Mass Transfer*, **109**:791–806, 2017.

[DNL10] SP Das, VS Nikolayev, Frédéric Lefèvre, B Pottier, S Khandekar, and Jocelyn Bonjour. "Thermally induced two-phase oscillating flow inside a capillary tube." *International Journal of Heat and Mass Transfer*, **53**(19-20):3905–3913, 2010.

[DS17] Bruce L Drolen and Christopher D Smoot. "Performance Limits of Oscillating Heat Pipes: Theory and Validation." *Journal of Thermophysics and Heat Transfer*, **31**(4):920–936, 2017.

[DWT22] Bruce L Drolen, Corey A Wilson, Brenton S Taft, Jonathan Allison, and Kevin W Irick. "Advanced Structurally Embedded Thermal Spreader Oscillating Heat Pipe Micro-Gravity Flight Experiment." *Journal of Thermophysics and Heat Transfer*, **36**(2):314–327, 2022.

[DYB17] J Doty, K Yerkes, L Byrd, J Murthy, A Alleyne, M Wolff, S Heister, and TS Fisher. "Dynamic thermal management for aerospace technology: review and outlook." *Journal of Thermophysics and Heat Transfer*, **31**(1):86–98, 2017.

[DYN17] Takurou Daimaru, Shuhei Yoshida, and Hiroki Nagai. "Study on thermal cycle in oscillating heat pipes by numerical analysis." *Applied Thermal Engineering*, **113**:1219–1227, 2017.

[Eld22] Jeff D Eldredge. "A method of immersed layers on Cartesian grids, with application to incompressible flows." *Journal of Computational Physics*, **448**:110716, 2022.

[Eve94] Geir Evensen. "Sequential data assimilation with a nonlinear quasi-geostrophic model using Monte Carlo methods to forecast error statistics." *Journal of Geophysical Research: Oceans*, **99**(C5):10143–10162, 1994.

[Eve09] Geir Evensen. *Data assimilation: the ensemble Kalman filter*. Springer Science & Business Media, 2009.

[HF05] Brian Holley and Amir Faghri. "Analysis of pulsating heat pipe with capillary wick and varying channel diameter." *International journal of heat and mass transfer*, **48**(13):2635–2651, 2005.

[Kal60] Rudolph Emil Kalman. "A new approach to linear filtering and prediction problems." 1960.

[Nik21] Vadim S Nikolayev. "Physical principles and state-of-the-art of modeling of the pulsating heat pipe: A review." *Applied Thermal Engineering*, **195**:117111, 2021.

[NN17] Iaroslav Nekrashevych and Vadim S Nikolayev. "Effect of tube heat conduction on the pulsating heat pipe start-up." *Applied Thermal Engineering*, **117**:24–29, 2017.

[NN19] Iaroslav Nekrashevych and Vadim S Nikolayev. "Pulsating heat pipe simulations: impact of PHP orientation." *Microgravity Science and Technology*, **31**(3):241–248, 2019.

[NS18] Reza Nemati and Mohammad Behshad Shafii. "Advanced heat transfer analysis of a U-shaped pulsating heat pipe considering evaporative liquid film trailing from its liquid slug." *Applied Thermal Engineering*, **138**:475–489, 2018.

[NYK21] Hyung Yun Noh, Aejung Yoon, and Sung Jin Kim. "Investigation into the effect of transverse condudction on the thermal performance of a flat-plate pulsating heat pipe." *International Journal of Heat and Mass Transfer*, **181**:121842, 2021.

[OWC21] Kimihide Odagiri, Kieran Wolk, Stefano Cappucci, Stefano Morellina, Scott Roberts, Andre Pate, Benjamin Furst, Eric Sunada, and Takuro Daimaru. "Three-dimensional heat transfer analysis of flat-plate oscillating heat pipes." *Applied Thermal Engineering*, **195**:117189, 2021.

[QM07] W Qu and HB Ma. "Theoretical analysis of startup of a pulsating heat pipe." *International Journal of Heat and Mass Transfer*, **50**(11-12):2309–2316, 2007.

[RLK15] Manoj Rao, Frédéric Lefèvre, Sameer Khandekar, and Jocelyn Bonjour. "Heat and mass transfer mechanisms of a self-sustained thermally driven oscillating liquid–vapour meniscus." *International Journal of Heat and Mass Transfer*, **86**:519–530, 2015.

[RMC21] Gautier Rouaze, Jackson B Marcinichen, Filippo Cataldo, Philippe Aubin, and John R Thome. "Simulation and experimental validation of pulsating heat pipes." *Applied thermal engineering*, **196**:117271, 2021.

[SFZ01] Mohammad B Shafii, Amir Faghri, and Yuwen Zhang. "Thermal modeling of unlooped and looped pulsating heat pipes." *J. Heat Transfer*, **123**(6):1159–1172, 2001.

[SI14] Raffles Senjaya and Takayoshi Inoue. "Oscillating heat pipe simulation considering dryout phenomena." *Heat and Mass Transfer*, **50**:1429–1441, 2014.

[SL14] Ramesh K Shah and Alexander Louis London. *Laminar flow forced convection in ducts: a source book for compact heat exchanger analytical data*. Academic press, 2014.

[TS17] Brent S Taft and Sally M Smith. "ASETS-II Oscillating Heat Pipe Space Flight Experiment: Ground Truth Results." In *ASME 2017 Heat Transfer Summer Conference*. American Society of Mechanical Engineers Digital Collection, 2017.

[Van99] Peter Jan Van Leeuwen. "Comment on "Data assimilation using an ensemble Kalman filter technique"." *Monthly Weather Review*, **127**(6):1374–1377, 1999.

[Won24] Zachary Wong. *Private communications*, 2024.

[ZFS02] Yuwen Zhang, A Faghri, and MB Shafii. "Analysis of liquid–vapor pulsating flow in a U-shaped miniature tube." *International Journal of Heat and Mass Transfer*, **45**(12):2501–2508, 2002.

[ZN23] Xiaolong Zhang, Vadim S Nikolayev, et al. "Physics and modeling of liquid films in pulsating heat pipes." *Physical Review Fluids*, **8**(8):084002, 2023.